2-mix

X-621-73-37
PREPRINT

NASA TM X- 66183

EMPIRICAL MODEL OF GLOBAL THERMOSPHERIC TEMPERATURE AND COMPOSITION BASED ON DATA FROM THE OGO-6 QUADRUPOLE MASS SPECTROMETER

A. E. HEDIN
H. G. MAYR
C. A. REBER
N. W. SPENCER
G. R. CARIGNAN

GODDARD SPACE FLIGHT CENTER
GREENBELT, MARYLAND

66

X-621-73-37

EMPIRICAL MODEL OF GLOBAL THERMOSPHERIC TEMPERATURE AND COMPOSITION BASED ON DATA FROM THE OGO-6 QUADRUPOLE MASS SPECTROMETER

A. E. Hedin

H. G. Mayr

C. A. Reber

N. W. Spencer

Goddard Space Flight Center, Greenbelt, Md.

and

G. R. Carignan

Space Physics Research Laboratory

University of Michigan, Ann Arbor, Michigan

December 1972

Goddard Space Flight Center
Greenbelt, Maryland

EMPIRICAL MODEL OF GLOBAL THERMOSPHERIC TEMPERATURE AND COMPOSITION BASED ON DATA FROM THE OGO-6 QUADRUPOLE MASS SPECTROMETER

ABSTRACT

An empirical global model for magnetically quiet conditions has been derived from longitudinally averaged N_2, O, and He densities by means of an expansion in spherical harmonics. The data were obtained by the OGO-6 neutral mass spectrometer and cover the altitude range 400 to 600 km for the period 27 June 1969 to 13 May 1971. The accuracy of the analytical description is of the order of the experimental error for He and O and about three times experimental error for N_2, thus providing a reasonable overall representation of the satellite observations. Two model schemes are used: one representing densities extrapolated to 450 km and one representing densities extrapolated to 120 km with exospheric temperatures inferred from N_2 densities. Using the best fit model parameters the global thermospheric structure is presented in the form of a number of contour plots.

EMPIRICAL MODEL OF GLOBAL THERMOSPHERIC TEMPERATURE AND COMPOSITION BASED ON DATA FROM THE OGO-6 QUADRUPOLE MASS SPECTROMETER

I. INTRODUCTION

This report presents a global thermosphere model for quiet magnetic conditions based on in situ measurements of N_2, O, and He obtained with the neutral particle quadrupole mass spectrometer [Carignan and Pinkus, 1968] carried aboard the OGO-6 satellite. The satellite was launched June 5, 1969 into an 82° inclination orbit with a 398 km perigee and 1100 km apogee and was operated until July, 1971. The reduction of the raw data to ambient densities makes use of the usual thermal transpiration equation in a moving coordinate system [Schultz et al., 1948; Horowitz and LaGow, 1957] and further includes corrections to the N_2 densities as a result of CO contributions to the mass 28 peak, and corrections to atomic oxygen densities as a result of oxygen surface adsorption, recombination, and desorption [Hedin et al., 1972a]. For each gas species a density value is determined every 9 seconds.

The uncertainty in N_2 and O densities as a result of noise in the data is always about 2% to 4%, but for He the uncertainty varies greatly (depending on the exact conditions) because of the generally low signal to noise ratio. Near perigee the uncertainty in density due to possible systematic errors in background subtraction and gas-surface interaction corrections is generally about 2% for N_2 and 6% for O (although it can be several times larger under very low

density conditions). These systematic errors increase with altitude, particularly above 500 km. No densities are used for which the total uncertainty (random and systematic) is estimated to exceed 25% for N_2 and O and 50% for He. In addition there is a laboratory calibration uncertainty of 10% to 15%.

The model described here is a more recent version of a model presented by Hedin et al. [1972b] at COSPAR. The principal changes are inclusion of: 8 hour local time components in the model formula; data from days with slightly higher magnetic activity; and data from the second year of satellite operation. The model is intended to provide in concise form as accurate a representation of the thousands of measured ambient densities as possible. At the same time, the model reveals many features, both familiar and novel, in the global distribution of the various gases which are inherent in the data but would not otherwise be easily seen.

II. DATA SELECTION AND COVERAGE

To eliminate strong magnetic activity effects data are selected from days which have a daily magnetic index, A_p, of 7 or less and a 3 hour magnetic index, a_p, less than 12 for that day and 6 hours earlier. The quiet days which have at least 8 orbits of good data reasonably distributed throughout the day are listed in Table 1. All the data obtained on a given day are grouped into 5° latitude bands (distinguishing also between data taken on north or south bound passes since these represent drastically different local times) and averaged over a 24 hour (universal time) period. All averages used in the model are based upon at least 20 density points. The averaging procedure eliminates longitudinal/UT effects [Hedin and Reber, 1972] in the data and reduces the amount of data handled, but does not eliminate local time effects since the orbit plane changes quite slowly with respect to the sun (2°/day).

For He there is a special data selection problem because it is observed that data from the second year of operation frequently differ by large factors from a model using first year data only. Raw data obtained during these periods are observed to fluctuate erratically in magnitude and the peak shape is not normal. Thus, an iterative procedure is used in fitting the data in which density points which differ from the model by more than a factor of two are eliminated and the remaining points refit.

The latitude and local time coverage of the data can be seen in Figures 1 and 2. In one year the latitude of perigee made three cycles around the globe

and (effectively) five diurnal cycles. Values of the mean (taken over three solar rotations) $F_{10.7}$ flux vary from 108 to 168 with an overall average near 150. Departures of the daily $F_{10.7}$ flux from the mean vary from -40 to +60. The overall average Ap value is 4. The number of days with good data available in the second year of operation is much less than in the first year because of telemetry and spacecraft problems.

III. MODEL FORMULA AND DATA FITTING

A. 450 km Densities

The composition is described in terms of density variations at 450 km, with an altitude dependence which assumes isothermal conditions (above 400 km) at any given time and location. Using a least squares technique, the average density data are fit with the following formula based on a spherical harmonic expansion (in geographic latitude-local time coordinates):

$$n(z, L) = n(450) \exp [G(L) - 1] \exp \left[- \frac{Mg (z - 450) (R_e + 450)}{R T_\infty (L) (R_e + z)} \right] \quad (1)$$

where

n = number density of a particular gas species [cm^{-3}]

z = altitude (km)

L = variable representing the geographical and geophysical parameters on which it is assumed density depends

M = molecular weight (gm/mole)

R_e = radius of the earth (6356.77 km)

g = acceleration of gravity (8.5529×10^{-3} km/sec^2 at 450 km)

R = gas constant (8.314×10^{-3} gm-km^2/mole-sec^2-deg)

T_∞ = exospheric temperature (°K)

G = spherical harmonic expansion as described in text

The function G (L) contains the basic information on the variation of density with selected geographic and solar activity parameters and is given in general as:

$$G(L) = 1 + \sum_{n=1}^{\infty} a_n^0 (t_d, F_{10.7}, A_p) P_n^0 (\theta) + \sum_{n=1}^{\infty} \sum_{m=1}^{n} a_n^m (t_d, F_{10.7}, A_p) P_n^m (\theta) \cos (m \omega \tau) + \sum_{n=1}^{\infty} \sum_{m=1}^{n} b_n^m (t_d, F_{10.7}, A_p) P_n^m (\theta) \sin (m \omega \tau) \quad (2)$$

where

a_n^m = parameters of the spherical harmonic expansion which are assumed to vary with day of the year (t_d), solar flux ($F_{10.7}$) and magnetic activity (A_p)

P_n^m = Legendre polynomials (not normalized)

θ = colatitude

ω = angular rate of earth rotation

τ = local solar time

The merit of an empirical model based on a spherical harmonic analysis is that these functions form a complete set which can, in principle, represent any degree of complexity in the data by systematically increasing the number of coefficients used. Furthermore, the spherical harmonics are approximate eigenfunctions in the thermosphere so that relatively few terms should be required, and analysis in terms of these components may aid in understanding the origin of various thermospheric variations [Reber, 1971; Mayr and Volland, 1971; Volland and Mayr, 1972; Reber and Hays, 1972].

The specific expansion of Equation 2 used to fit the data for the current model is as follows:

$$G = 1$$

(time independent) $+ a_{20} P_{20} + a_{40} P_{40}$

(primary $F_{10.7}$ effect) $+ F_0$

(magnetic activity) $+ (k^a_{00} + k^a_{20} P_{20}) \Delta A$

(symmetrical annual) $+ (c^1_{00} + c^1_{20} P_{20}) \cos \Omega (t_d - t^{C1}_{00})$

(symmetrical semiannual) $+ (c^2_{00} + c^2_{20} P_{20}) \cos 2 \Omega (t_d - t^{C2}_{00})$

(asymmetrical annual) $+ (c^1_{10} P_{10} + c^1_{30} P_{30} + c^1_{50} P_{50})(1 + F_1) \cos \Omega (t_d - t^{C1}_{10})$

(asymmetrical semiannual) $+ c^2_{10} P_{10} \cos 2 \Omega (t_d - t^{C2}_{10})$

(diurnal)
$$+ [a_{11} P_{11} + a_{31} P_{31} + a_{51} P_{51}$$
$$+ (c^1_{11} P_{11} + c^1_{21} P_{21}) \cos \Omega (t_d - t^{C1}_{10})] (1 + F_1) \cos \omega\tau$$
$$+ [b_{11} P_{11} + b_{31} P_{31} + b_{51} P_{51}$$
$$+ (d^1_{11} P_{11} + d^1_{21} P_{21}) \cos \Omega (t_d - t^{C1}_{10})] (1 + F_1) \sin \omega\tau$$

(semidiurnal)
$$+ [a_{22} P_{22} + c^1_{32} P_{32} \cos \Omega (t_d - t^{C1}_{10})] (1 + F_1) \cos 2\omega\tau$$
$$+ [b_{22} P_{22} + d^1_{32} P_{32} \cos \Omega (t_d - t^{C1}_{10})] (1 + F_1) \sin 2\omega\tau$$

(terdiurnal)
$$+ a_{33} P_{33} (1 + F_1) \cos 3\omega\tau$$
$$+ b_{33} P_{33} (1 + F_1) \sin 3\omega\tau \qquad (3)$$

where

$$P_{nm} = P_n^m (\cos \theta)$$

$$F_0 = f_{00}^{a1} \Delta F + f_{00}^{a2} (\Delta F)^2 + \overline{f_{00}^{a1}}\ \overline{\Delta F}$$

$$F_1 = f_1 F_0$$

$$\Delta F = F_{10.7} - \overline{F_{10.7}}$$

$$\overline{\Delta F} = \overline{F}_{10.7} - 150.$$

$$\Delta A = A_p - 4.$$

$F_{10.7}$ = 10.7 cm flux one day earlier (10^{-22} watt - m^{-2} - cps^{-1})

$\overline{F}_{10.7}$ = 3 solar rotation average of $F_{10.7}$

A_p = 24 hour average of magnetic index, a_p, with a six hour lag

$\Omega = 2\pi/365$ ($days^{-1}$)

$\omega = 2\pi/24$ (hrs^{-1})

t_d = daycount (days)

τ = local solar time (hrs)

The significance of the various terms in Equation 3 is indicated briefly in parenthesis at the left. The expansion includes local time independent, diurnal, semidiurnal, and terdiurnal terms plus terms representing the annual, semiannual, solar flux, and magnetic activity variations. For convenience, terms higher than the eight hour local time harmonic are not included. However, it has been shown that the first three harmonics are sufficient to fit incoherent scatter data reasonably well

[Salah and Evans, 1972]. The form of the $F_{10.7}$ correlation used is similar to that of Jacchia [1971] except that allowance is made for a possible nonlinearity in the correlation with the 27 day $F_{10.7}$ variation as suggested by incoherent scatter data [Waldteufel and Cogger, 1971]. Following Jacchia it is also assumed that changes in the diurnal and annual temperature amplitudes resulting from $F_{10.7}$ variations are strictly proportional to the changes in mean temperature, but the same assumption is not necessarily true for thermospheric densities which depend strongly and nonlinearly on temperature through the hydrostatic equation. Thus it is necessary to introduce the parameter f_1 when determining the 450 km densities for N_2 and O (f_1 did not differ significantly from unity for He). When determining exospheric temperatures and 120 km densities, as described in the next section, f_1 is assumed to equal one. The correlation with A_p is assumed to be linear, as the range of A_p included in this quiet time model is quite small. While the A_p used in the fitting is a daily average based on a six hour lag as adopted in the Jacchia models, the difference in calculating densities using the normal daily A_p is insignificant. The possibility of a latitude variation of the magnetic activity effect was included. Combining Equations 1 and 3 there are 37 unknown parameters to be determined by fitting the data.

The temperature (T_∞) needed in Equation 1 is determined from the N_2 data in a manner to be described below, but is not critical to determining 450 km densities since this altitude is near the average altitude of the measurements.

Tests were made using both temperatures from Jacchia [1965] and a constant temperature to verify that the 450 km density determination is relatively insensitive to the exospheric temperature.

B. Inferred Exospheric Temperatures and 120 km Densities

Adopting a method analogous to that employed by Jacchia [1965], the temperature and N_2 density are fixed at 120 km and the exospheric temperature necessary to calculate the measured densities is then determined using analytic density profiles suggested by Walker [1965] based on a temperature profile suggested by Bates [1959]:

$$T(z, L) = T_\infty(L) - (T_\infty(L) - T_{120}) \exp[-s(z - 120)] \tag{4}$$

$$n(z, L) = n(120)\, D(z, T_\infty(L), s) \tag{5}$$

$$D(z, T_\infty(L), s) = \left(\frac{1 - a}{1 - a\, e^{-\sigma\xi}}\right)^{1+\alpha+\gamma} \exp[-\sigma\gamma\xi] \tag{6}$$

where

$$\sigma = s + .00015$$

$$a = 1 - T_{120}/T_\infty(L)$$

$$\xi = (z - 120)(R_E + 120)/(R_E + z)$$

$$\gamma = M g /(\sigma R T_\infty(L))$$

$$T_\infty(L) = \bar{T}_\infty\, G(L)$$

T_{120} = temperature at 120 km (355°K)

s = temperature gradient parameter

g_e = acceleration of gravity at 120 km (9.44663×10^{-3} km/sec^2)

$\bar{T}_\infty$ = average exospheric temperature

The temperature calculation is based on the N_2 density, rather than O or He, because this species is probably most nearly in diffusive equilibrium [Reber, 1971; Mayr and Volland, 1971; Mayr and Volland, 1972a] when dynamical processes are considered. In addition, variations in the eddy diffusion will have the least effect on the nitrogen concentration because its molecular weight is approximately the mean molecular weight at the turbopause. However, the average temperature ($\bar{T}_\infty$) needed to fit the measurements is not arbitrary, because the measurements are made at different altitudes, and there is an average temperature which will best fit the density data. The capability of determining an average temperature independent of the 120 km boundary conditions was maintained by allowing the 's' parameter to be determined by the least squares fit. Combining Equations 3, 5, and 6 there are 37 unknown parameters to be determined by fitting the nitrogen data, including $\bar{T}_\infty$, s, and the parameters in function G.

It would be possible in principle to determine independently the global temperature distribution from scale height information alone and a preliminary attempt indicated that results would be in rough agreement with the temperature distribution obtained using the diffusive equilibrium model of Equation 5. However, the uncertainty limits were so large that it was doubtful that useful additional temperature variation information could be obtained from the scale height.

B

Using the temperatures inferred from the nitrogen data, the average densities and variations at 120 km needed to reproduce the measurements of O and He are determined by using a slight modification of Equation 5:

$$n(z, L) = n(120)\, D(z, T_\infty(L), s) \exp[G(L) - 1] \qquad (7)$$

where the density variations are again introduced through the G function of Equation 3. There are 36 unknown parameters to be determined including n (120).

It should be noted that the 450 km density model and the diffusive equilibrium model starting at 120 km can (in principle) represent the measured densities equally well, as the model parameters are determined independently by fitting the measured data. However, the inferred exospheric temperature and absolute densities at 120 km are dependent on the existence of diffusive equilibrium and the assumed boundary conditions. The variations in composition at 120 km are, nevertheless, a convenient way of illustrating departure from fixed boundary diffusive-equilibrium models; moreover, density ratios inferred at 120 km are less dependent on errors in exospheric and boundary temperatures than are the absolute densities at 120 km.

IV. MODEL PARAMETER RESULTS AND ACCURACY

The model parameters for N_2, O, and He densities at 450 km are given in Table 2 and those for O and He densities at 120 km and exospheric temperatures in Table 3. Also given are the estimated standard deviations for the parameters and a parameter indicating the overall quality of the fit:

$$Q_f = \left\{ \sum_i \left[\frac{(n_m^i - n_c^i)}{\sigma_m^i} \right]^2 \Big/ (N_d - N_p) \right\}^{1/2} \tag{8}$$

where

n_m^i = i^{th} measured density

n_c^i = i^{th} calculated density

σ_m^i = estimated measurement error

N_d = number of data points

N_p = number of parameters

The least squares fits are carried out using about 1000 data points randomly selected from a data base about twice as large.

The temperature at 120 km is fixed at 355°K and the N_2 density at 120 km is chosen to provide an N_2 density at 150 km very close to that recommended by Van Zahn [1970] and used by Jacchia [1971]. The inferred average O to N_2 density ratio at 150 km turns out to be about 72% of that recommended by Von Zahn. However, in light of the errors in the various measurement methods, the variability of the densities, the assumptions used in extrapolating the

satellite measurements, and the possible error in the assumed 120 km temperature, this small disagreement in the oxygen to nitrogen ratio is not significant. A total assessment of various measurements in the lower thermosphere and their consistency with the upper thermosphere measurements is not attempted in this model.

The quality of the model fits to the data is examined by using the coefficients from Table 3 and plotting the measured to calculated density ratios as a function of time from perigee, latitude, local time, solar flux, A_p, and day-count, as shown in Figures 3 to 5. In Figures 6 to 8 the residuals are represented by symbols in a latitude versus local time plot. In general, there are no large systematic differences in the fit. Examination of the plots of measured to calculated density ratios versus time from perigee indicates that the density data have been reasonably corrected for gas-surface interactions. The generally good fit does not necessarily mean that all significant terms have been found, particularly when interactions between variables are considered. For example, Figures 6 to 8 show that while the overall distribution of points in latitude-local time space is good, the same is not true at all seasons. The data coverage for N_2 and O is much better during summer than winter and the converse is true for helium. This will reduce the reliability of the model in winter for N_2 and O, in the summer for He, and of the seasonal interaction terms.

The question of the validity of individual and combinations of parameters, and thus the proper decomposition into the various components, is very difficult to answer completely. In general, one can say that since latitude profiles are the basic data input to the model, the model should predict latitude profiles with the most accuracy. While local time variations are basically derived from data on many different days, the lack of systematic residuals as a function of local time indicates that these variations should be reasonably well represented on average but not necessarily in their seasonal variations. The least reliable coefficients are expected to be those connected with the symmetrical annual and the symmetrical and asymmetrical semiannual components since the data base is not long compared to these cycles. There is also the possible confusion of true annual and semiannual components with these frequencies in the mean $F_{10.7}$ variation. While the standard deviations calculated for each coefficient give some guidance, they cannot completely account for a lack of uniform data sampling in all coordinates.

The possibility of changes in the model coefficients from year to year was examined by dividing the data into two samples and fitting separately. The results for the temperature coefficients are given in Table 4. As expected, the coefficients relating to the semiannual and symmetrical annual components have changed the most, while the majority are quite stable.

The probable accuracy of the inferred average temperature was tested by arbitrarily changing the average temperature by 50°K and 100°K and refitting N_2 density for the remaining coefficients. The change in Q_f (Equation 8) and the density ratio versus time from perigee plot indicated that a 50°K change would not be entirely unreasonable, but that a 100°K change produced fairly marked deviations from the best fit. Another consideration is that if the highest altitude densities (about three scale heights above perigee) have a systematic error of 25%, this would roughly translate to a 80°K error. A test fit of oxygen density leaving T_∞ as a free parameter produced a temperature about 50° higher than from the nitrogen data. Because there is some difference between exospheric temperature and the temperature near 450 km, the inferred exospheric temperature does depend somewhat on the s parameter. If s were .025, the inferred exospheric temperature would be 10° lower; and if s were .015, the inferred exospheric temperature would be 40° higher. The best estimate is that the average temperature is accurate to ±50°K.

The accuracy with which the inferred temperature variations represent real temperature variations depends on the assumed constancy of the 120 km N_2 density and temperature. This assumption appears, however, to be a reasonable first approximation that can be modified later to provide better agreement with other measurements. A 10% variation in 120 km density would result in roughly a 1.5% error in exospheric temperature variations and a 10% variation in 120 km temperature would result in roughly a 4% error in exospheric temperature variations. A variation of N_2 density during one day at 140 km on the order of

30% and temperature on the order of 20% was measured by Spencer et al. [1969] in a series of rocket flights. Semidiurnal temperature amplitudes at 120 km on the order of 10% have been reported by Salah and Evans [1972]. Theoretically, Volland and Mayr [1970] predict a 120 km diurnal temperature amplitude of 5% and a density amplitude of 10%. Seasonal variations in temperature at 120 km of about 10% have been reported by Waldteufel [1970], with a level of relatively constant density at 130 km. Mayr and Volland [1972b] predict annual amplitudes at 120 km of 8% in temperature and 20% in N_2 density.

The accuracy of the inferred oxygen and helium variations at 120 km depends on both the accuracy of the inferred temperature variations and the diffusive equilibrium assumption. Because of mass motions it is expected theoretically that there will be departures from diffusive equilibrium in the lower thermosphere, particularly for minor constituents like helium.

V. GLOBAL THERMOSPHERIC STRUCTURE

The model coefficients given in Tables 2 and 3 can be used to predict atmospheric structure for various conditions. Predictions for altitudes, solar activity conditions, etc., which are beyond the data base used in generating the model must obviously be used with caution. A set of plots of exospheric temperature, densities at 120 km, and densities at 450 km are presented in Figures 9 through 14. By use of the plots for the individual components of the model a graphical solution for many situations can be constructed.

The OGO-6 model shows a number of departures from previous empirical models based on total density measurements obtained from satellite drag [Jacchia, 1965; Jacchia, 1971]. Among these are the morning maximum for He, the high latitude of the diurnal temperature bulge position for solstice conditions, the seasonal variation of the O to N_2 density ratio with a 400°K summer to winter temperature difference, and the 1600 hour maximum for N_2 with an extended bulge in latitude. These effects will be discussed in separate reports. The differences from drag models undoubtedly arise in part because composition and temperature cannot be uniquely determined from total density measurements alone [Stein and Walker, 1965] and because of the smoothing inherent in the method of determining the density from variations in a satellite's orbit [Jacchia, 1971].

The total densities predicted by the OGO-6 model are compared with those of the J71 model [Jacchia, 1971] in Figure 15. The average density is 17%

higher than J71, certainly within the overall measurement error and limitations of model predictions. The shape of the diurnal curve for 45° latitude is in quite good agreement with J71 and the equatorial curve is in fair agreement, although the OGO-6 model has a slightly later afternoon maximum. The seasonal variation compares well with J71, particularly north of -45° latitude.

Measurements of temperature [Salah and Evans, 1972] made during the same time period as the OGO-6 measurements are compared in Figure 16. The average OGO-6 inferred temperature is about 7% higher than the incoherent scatter measurements. The annual variations are in quite good agreement and are over twice those predicted by J71. The diurnal variations show quite good agreement except for the early morning hours of winter, which is not too surprising considering the lack of satellite data in this area (Figure 6).

VI. ACKNOWLEDGEMENTS

We are indebted to the many people in the Space Physics Research Laboratory of the University of Michigan, particularly W. H. Pinkus and D. R. Taeusch, and in the Laboratory for Planetary Atmospheres of the Goddard Space Flight Center, particularly D. N. Harpold and J. E. Cooley, who contributed to the success of this experiment.

REFERENCES

Bates, D. R., Some problems concerning the terrestrial atmosphere above about the 100 km level, Proc. Roy. Soc. London, A253, 451-462, 1959.

Carignan, G. R. and W. H. Pinkus, OGO-F04 experiment description, University of Michigan Technical Note 08041-3-T, 1968.

Hedin, A. E., B. B. Hinton, and G. A. Schmitt, Role of Gas Surface Interactions in the reduction of OGO-6 neutral gas particle mass spectrometer data, NASA X-621-72-90, 1972a.

Hedin, A. E., H. G. Mayr, C. A. Reber, G. R. Carignan, and N. W. Spencer, A global empirical model of thermospheric composition based on OGO-6 mass spectrometer measurements, presented at the XV meeting of COSPAR, Madrid, Spain, 1972b.

Hedin, A. E. and C. A. Reber, Longitudinal variations of thermospheric composition indicating magnetic control of polar heat input, J. Geophys. Res., 77, 2871-2879, 1972.

Horowitz, R. and H. E. LaGow, Upper air pressure and density measurements from 90 to 220 km with the Viking 7 rocket, J. Geophys. Res. 62, 57-78, 1957.

Jacchia, L. G., Static diffusion models of the upper atmosphere with empirical temperature profiles, Smithson. Contr. Astrophys., 8, 215, 1965.

Jacchia, L. G., Revised static models of the thermosphere and exosphere with empirical temperature profiles, Smithsonian, Astrophys. Ob. Special Report 332, 1971.

Mayr, H. G. and H. Volland, Semiannual variations in the neutral composition, Ann. Geophys., 27, 513-522, 1971.

Mayr, H. G. and H. Volland, Diffusion model for the phase delay between thermospheric density and temperature, J. Geophys. Res., 77, 2359-2367, 1972a.

Mayr, H. G. and H. Volland, Theoretical model for the latitude dependence of the thermospheric annual and semiannual variations, J. Geophys. Res., 77, 1972b.

Reber, Carl A., Thermospheric wind effects on the global distribution of helium in the earth's upper atmosphere, NASA X-621-71-480, 1971.

Reber, C. A. and P. B. Hays, Thermospheric wind effects on the distribution of minor gases in the earth's upper atmosphere, submitted for publication to J. Geophys. Res., 1972.

Salah, J. E. and J. V. Evans, Measurements of thermospheric temperature by incoherent scatter radar, presented at the XV meeting of COSPAR, Madrid, Spain, 1972.

Schultz, F. V., N. W. Spencer and A. Reifman, Atmospheric pressure and temperature measurements between altitudes of 40 and 110 km, University of Michigan Research Institute, Upper Atmosphere Report No. 2, 1948.

Spencer, N. W., G. P. Newton, G. R. Carignan, and D. R. Taeusch, Thermosphere temperature and density variations with increasing solar activity, Space Research X, North-Holland Publishing Co., Amsterdam, 1970.

Stein, J. A. and J. C. G. Walker, Models of the upper atmosphere for a wide range of boundary conditions, J. Atmos. Sci., 22; 11, 1965.

Volland, H. and H. G. Mayr; A theory of the diurnal variations of the thermosphere, Ann. Geophys., 26, 907, 1970.

Volland, H. and H. G. Mayr, A three dimensional model of thermospheric dynamics (Heat input and eigenfunctions), J. Atmos. Terr. Phys., 34, 1745-1768, 1972.

von Zahn, U., Neutral air density and composition at 150 km, J. Geophys. Res., 75, 5517, 1970.

Waldteufel, P., A study of seasonal changes in the lower thermosphere and their implications, Planet. Space Sci., 18, 741-748, 1970.

Waldteufel, P. and L. Cogger, Measurements of the neutral temperature at Arecibo, J. Geophys. Res., 76, 5322-5336, 1971.

Walker, James C. G., Analytic representation of upper atmosphere densities based on Jacchia's static diffusion models, J. Atmos. Sci., 22, 462, 1965.

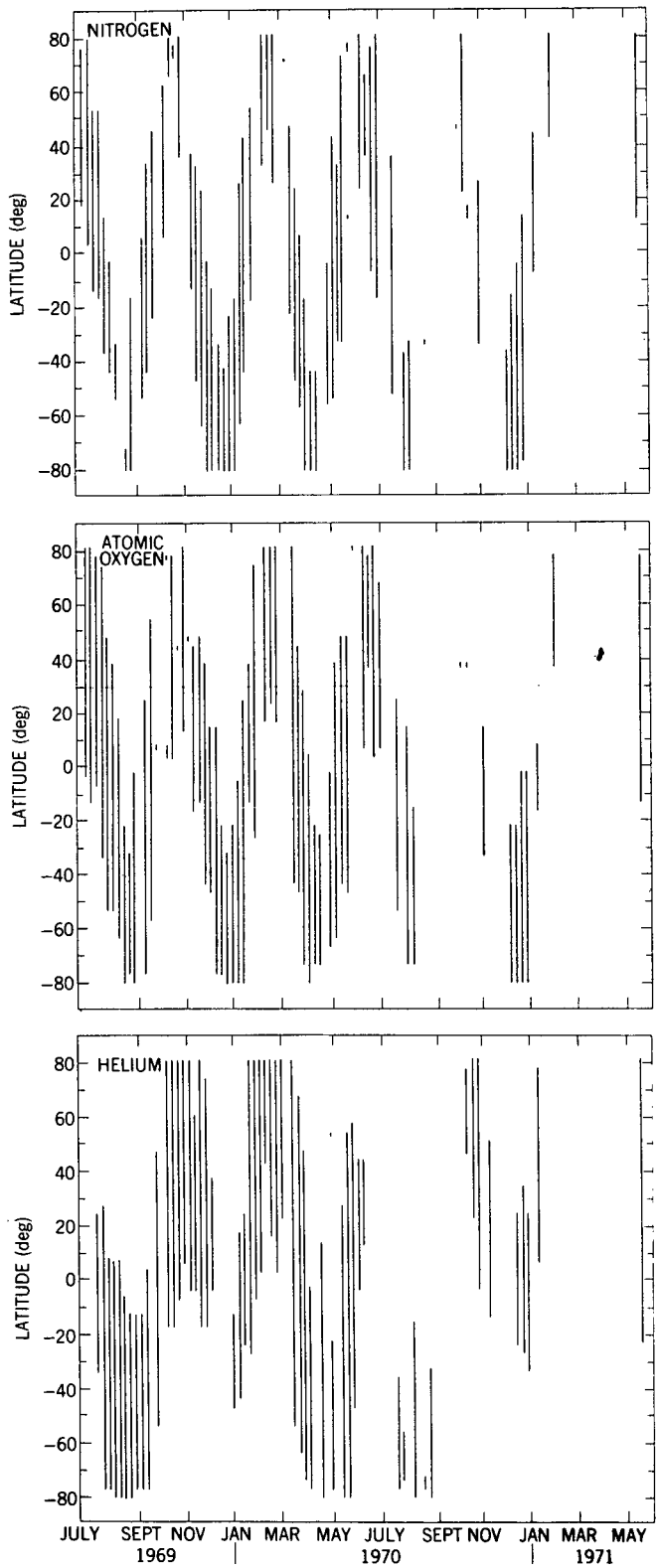

Figure 1. Geographic latitude coverage of available N_2, O, and He density data as a function of day.

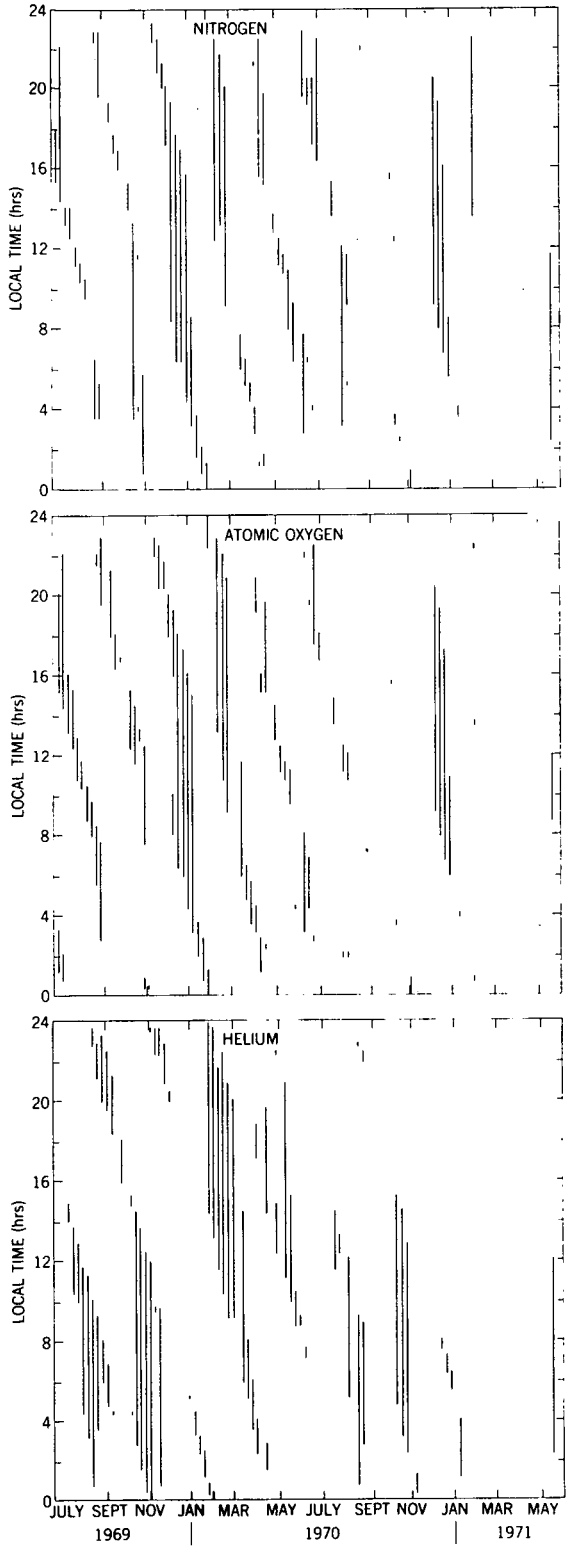

Figure 2. Local time coverage of available N_2, O, and He density data as a function of day.

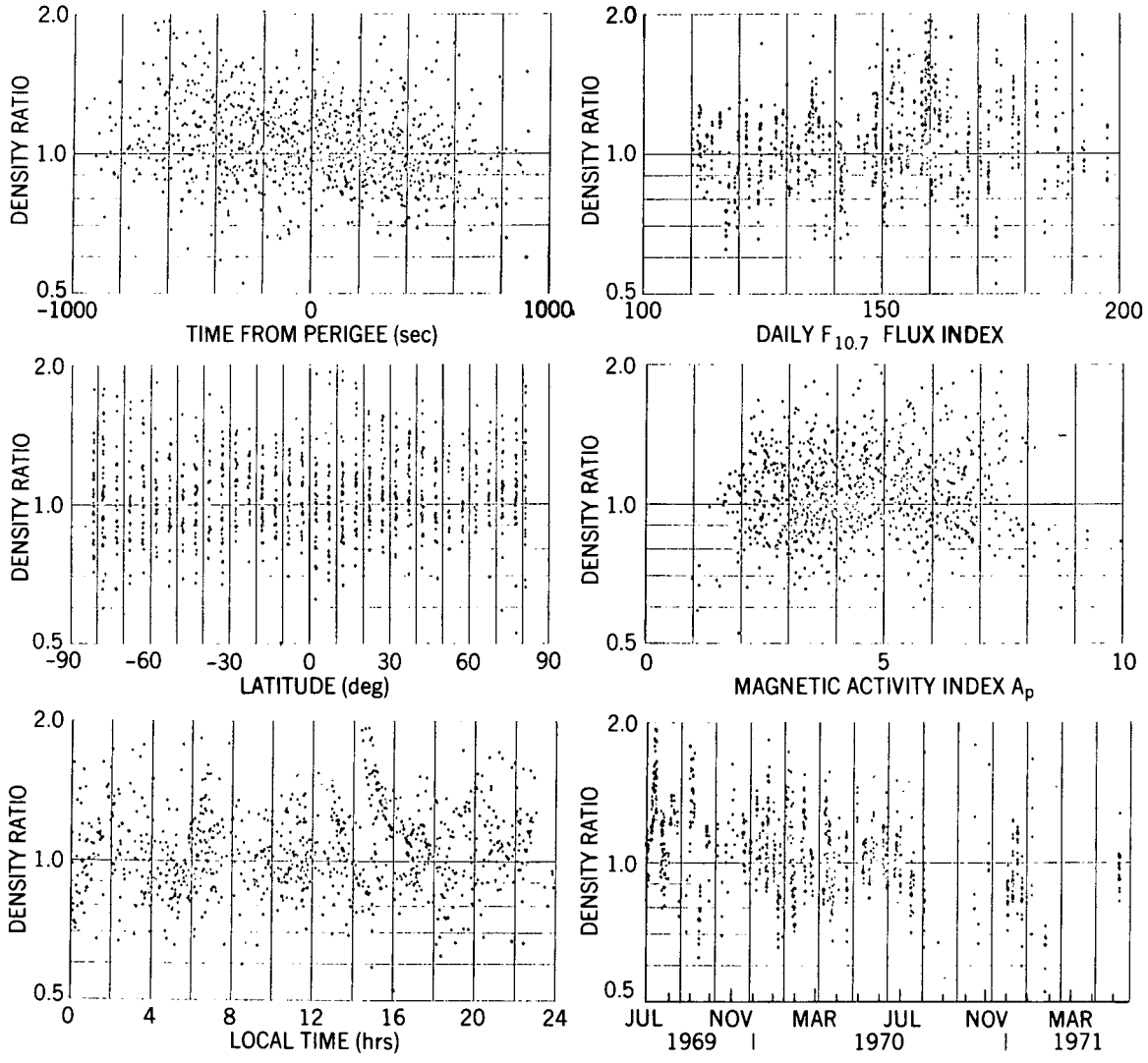

Figure 3. Ratio of the measured N_2 density to the model N_2 density as a function of time from perigee, geographic latitude, local time, $F_{10.7}$ solar flux, magnetic index A_p and day of year.

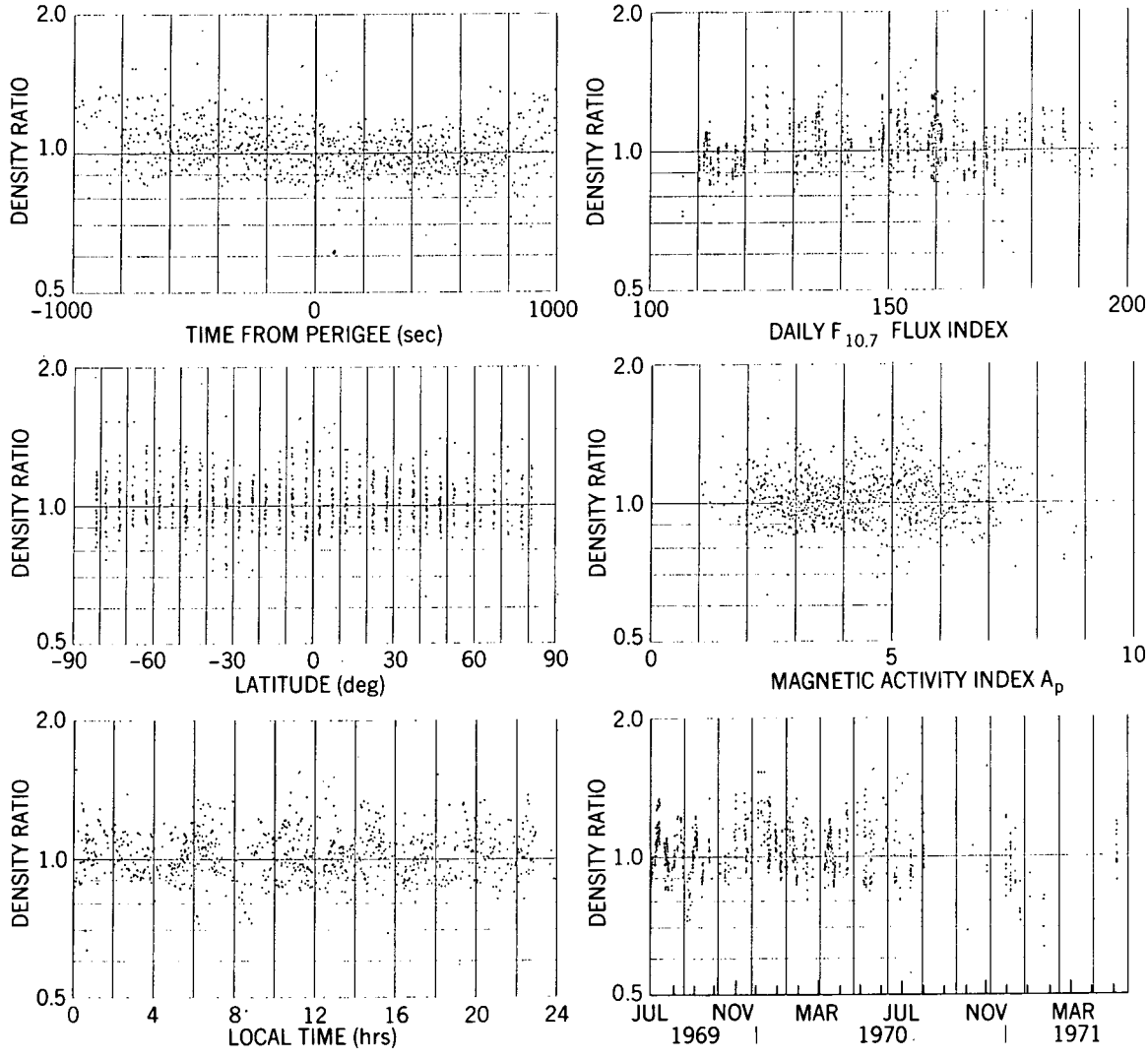

Figure 4. Ratio of the measured O density to the model O density plotted in the same format as Figure 3.

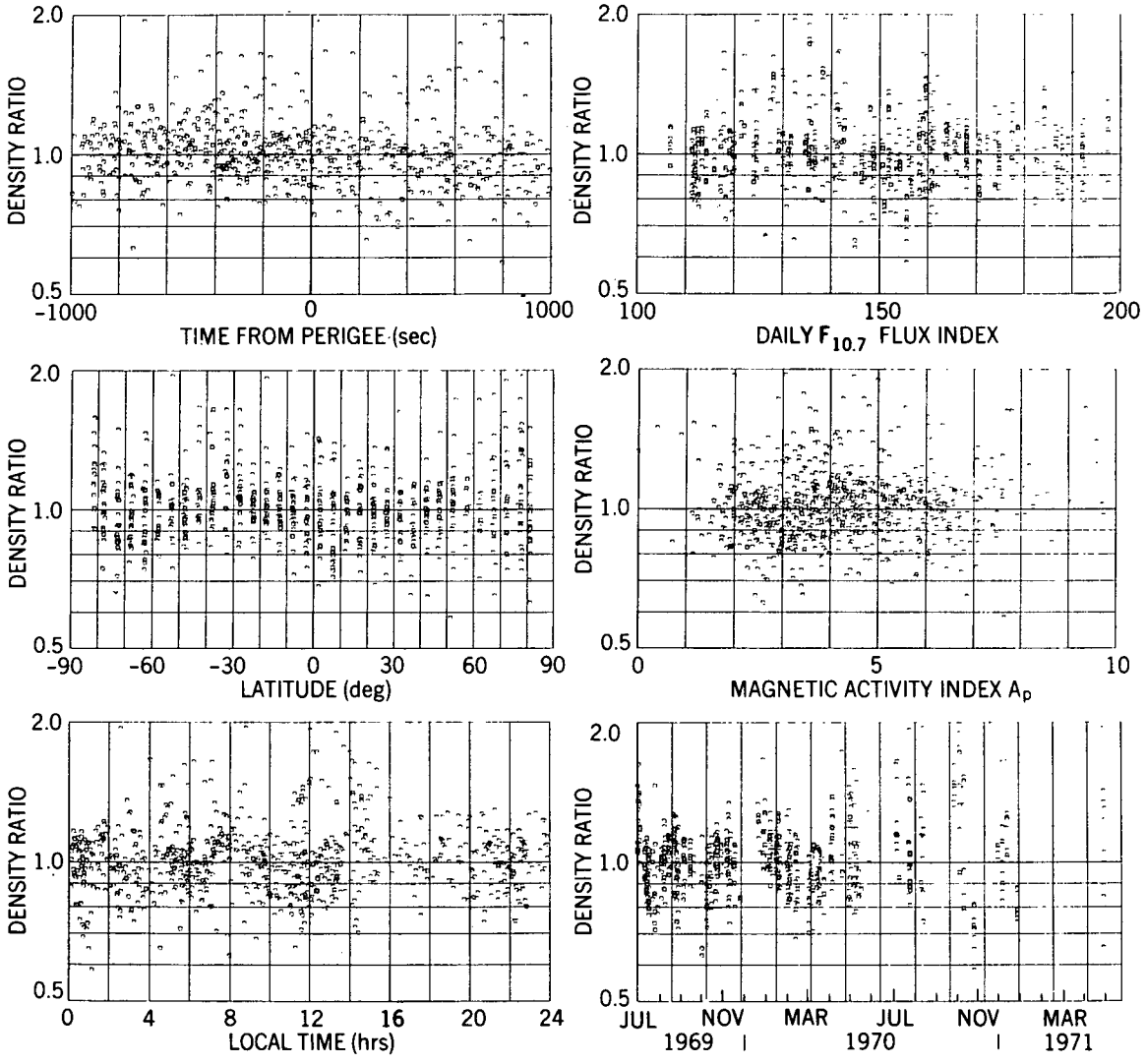

Figure 5. Ratio of the measured He density to the model He density plotted in the same format as Figure 3.

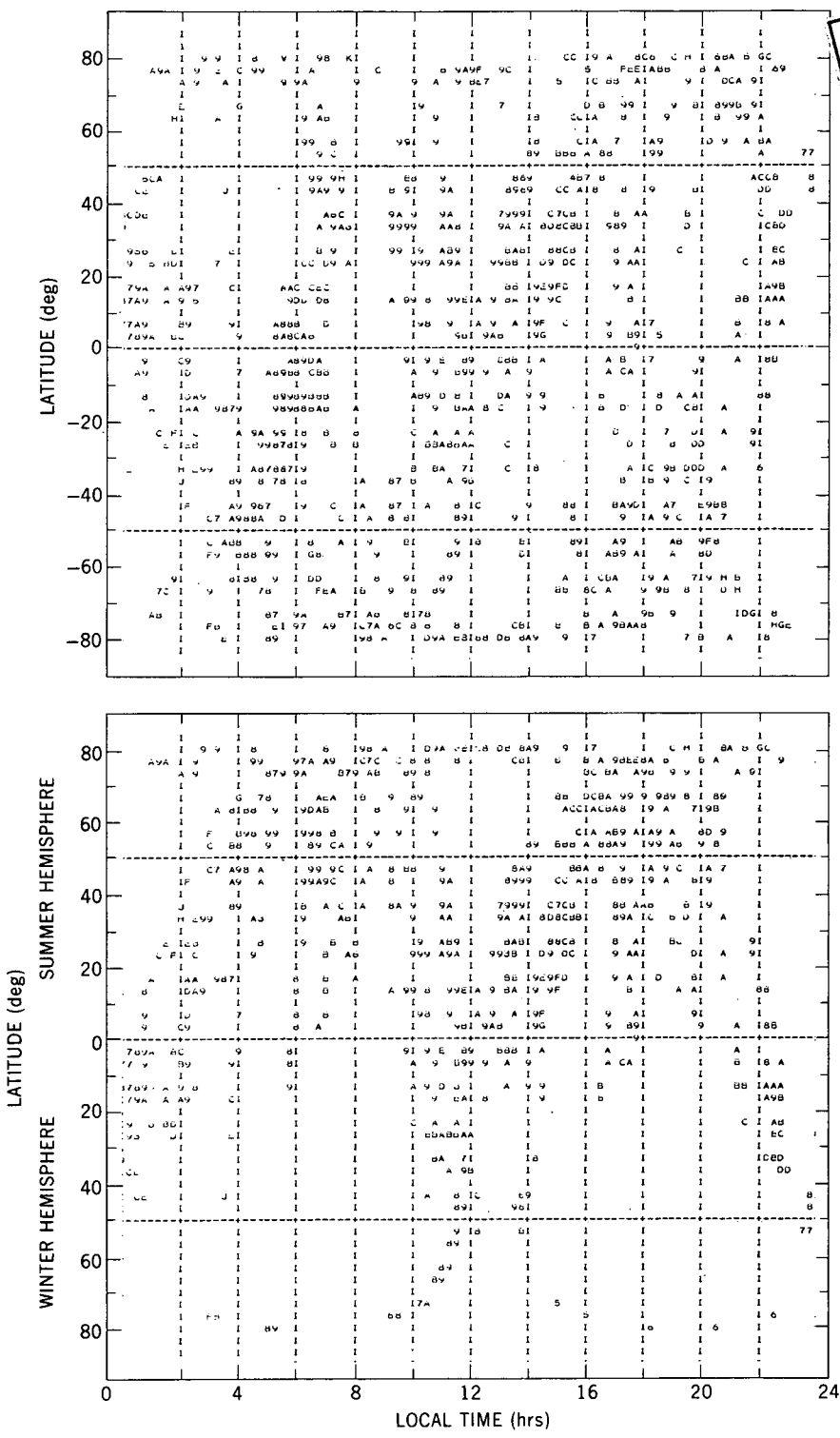

Figure 6. Ratio of the measured N_2 density to the model N_2 density plotted in a latitude-local time coordinate system. The plotted letter A indicates a ratio of 1.0, B a ratio of 1.1, 9 a ratio of .9, and so on. In the lower half of the figure the data have been restricted to ±45 days from the solstices and plotted in the respective summer and winter hemispheres.

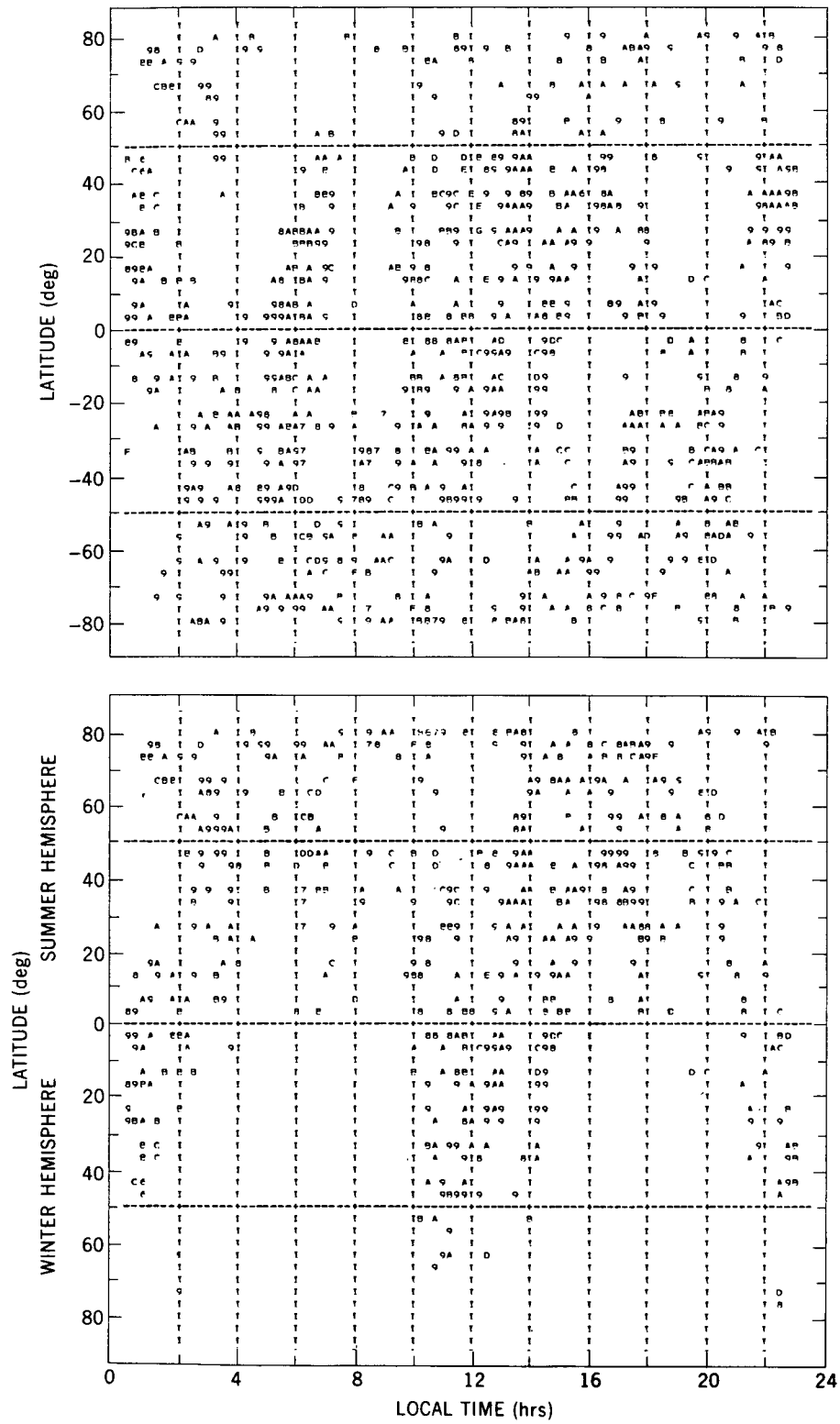

Figure 7. Ratio of the measured O density to the model O density plotted in the same format as Figure 6.

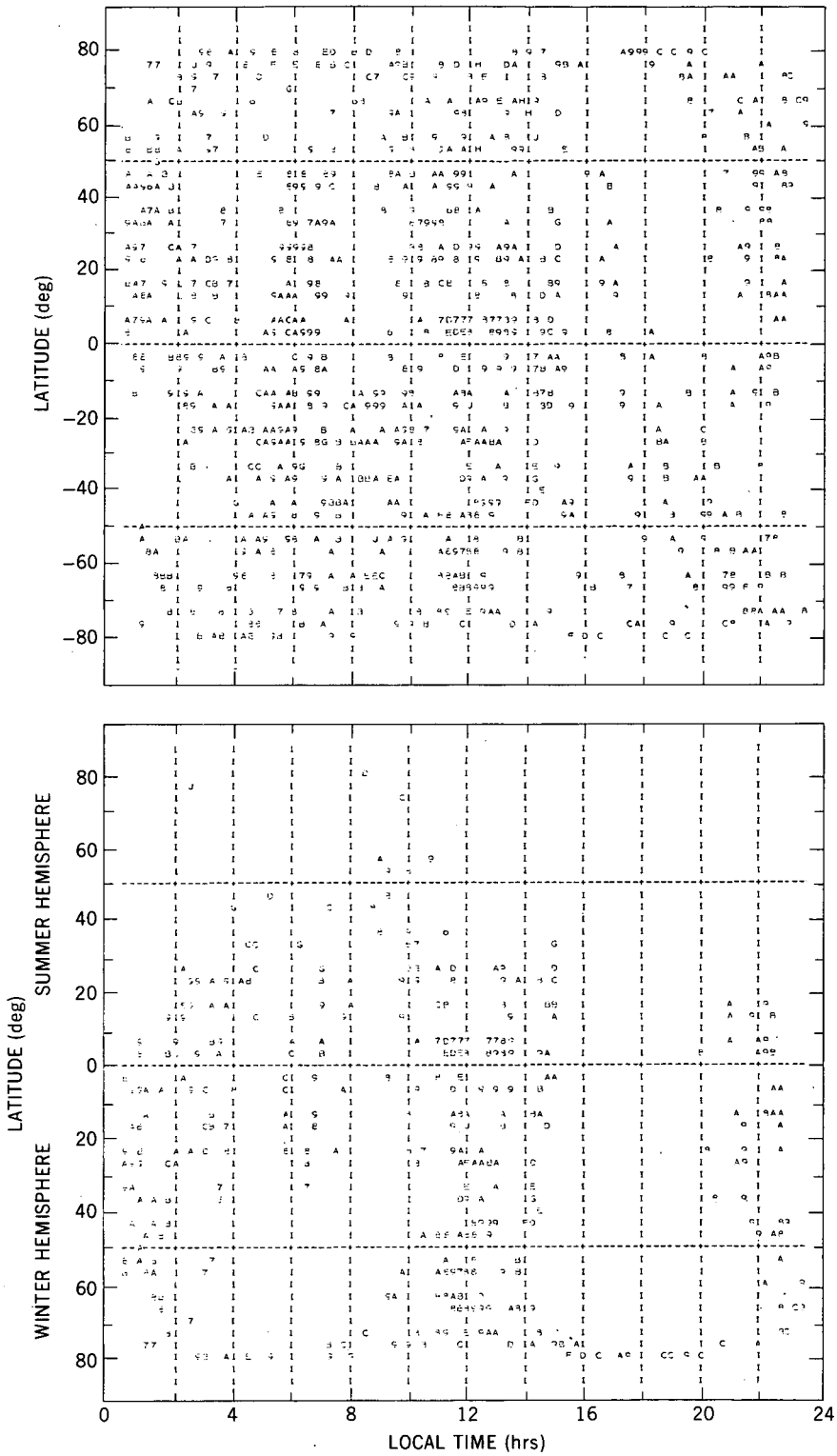

Figure 8. Ratio of the measured He density to the model He density plotted in the same format as Figure 6.

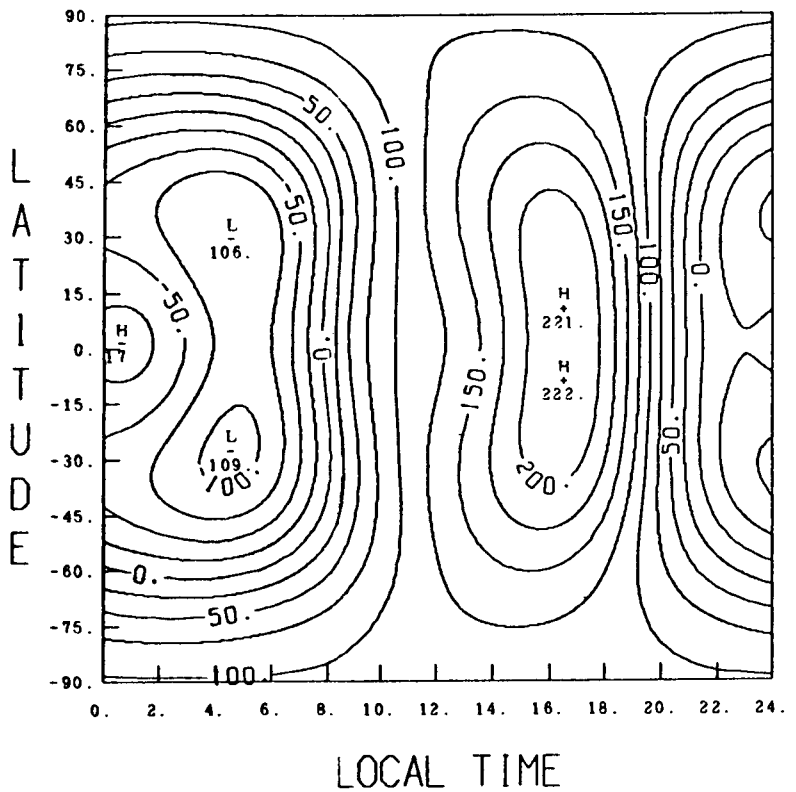

Figure 9a. Contour plot of departures of inferred exospheric temperature from the global mean (1098 K) for September equinox conditions assuming an $F_{10.7}$ of 150 and an A_p of 4.

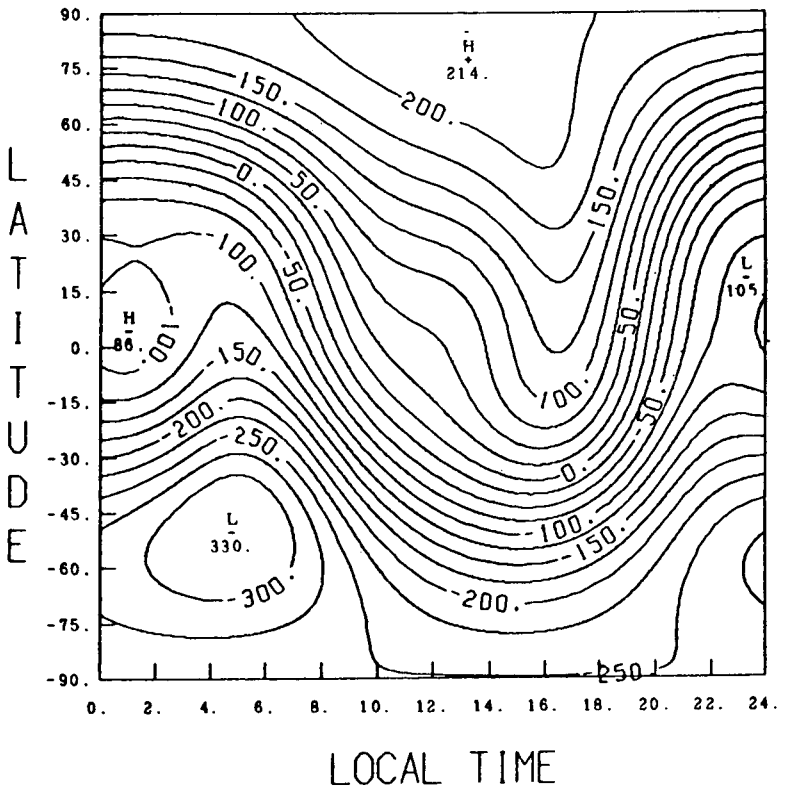

Figure 9b. Same as 9a for June solstice conditions.

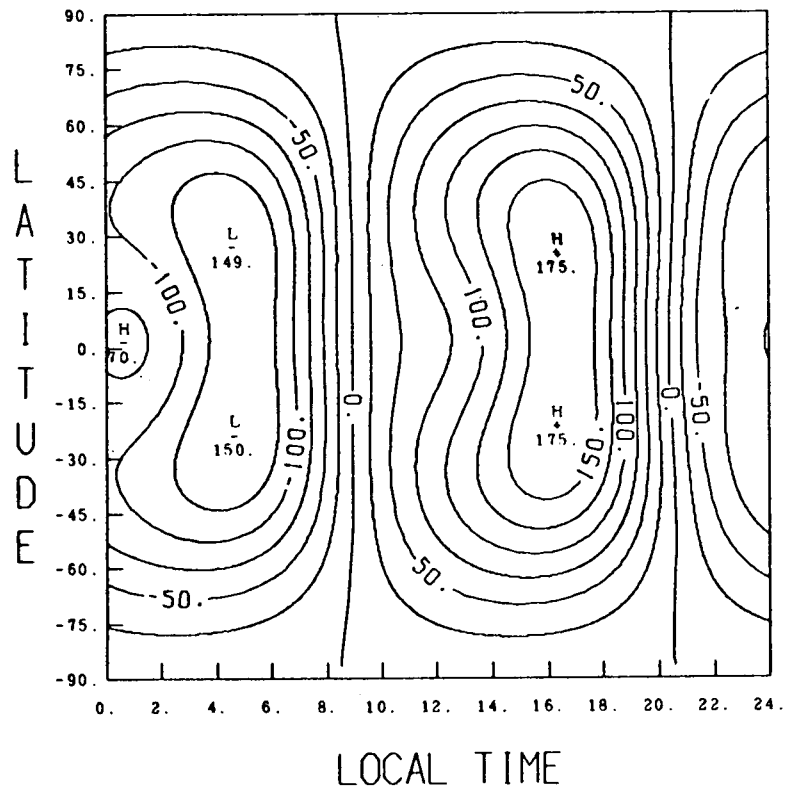

Figure 9c. Contour plot of departures of inferred exospheric temperature from the global mean (1098°K) using the diurnal, semidiurnal, and terdiurnal components only for September equinox conditions (assuming an $F_{10.7}$ of 150).

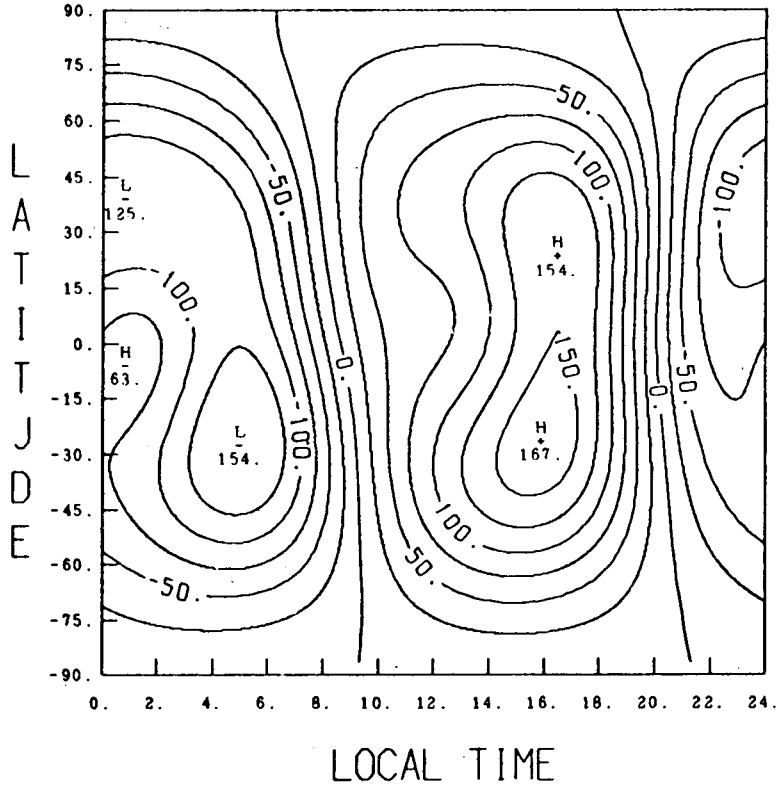

Figure 9d. Same as 9c for June solstice conditions.

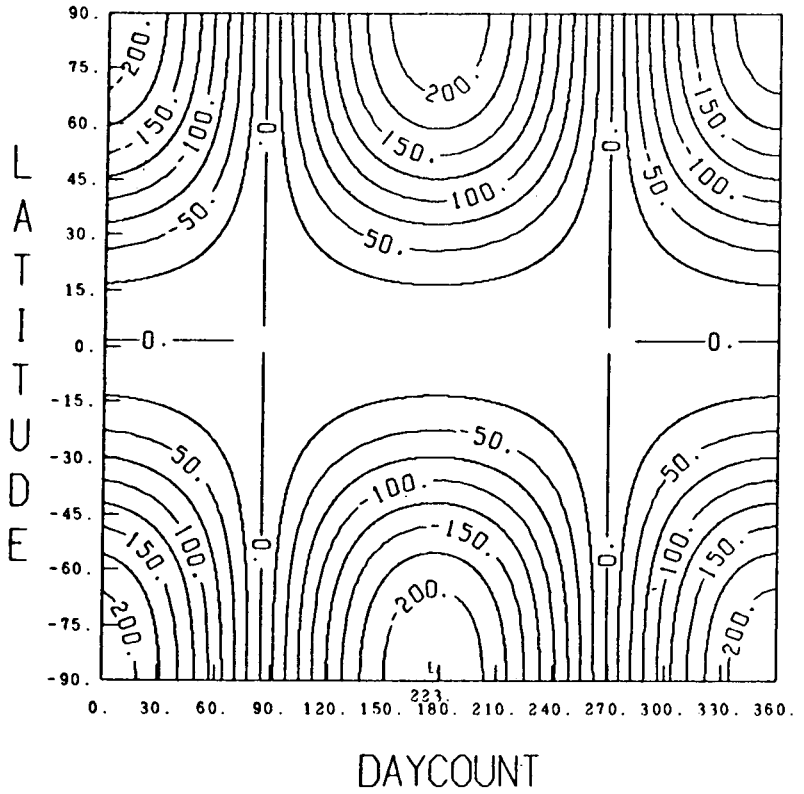

Figure 9e. Contour plot of departures of inferred exospheric temperature from the global mean (1098°K) using the asymmetrical annual component only (assuming an $F_{10.7}$ of 150).

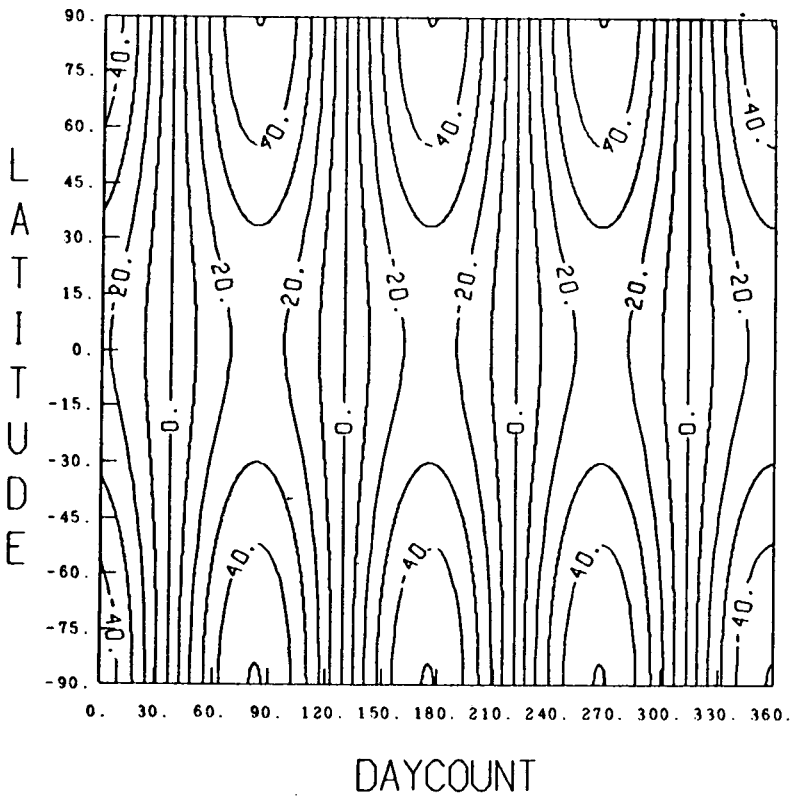

Figure 9f. Same as 9e using the symmetrical semiannual component only.

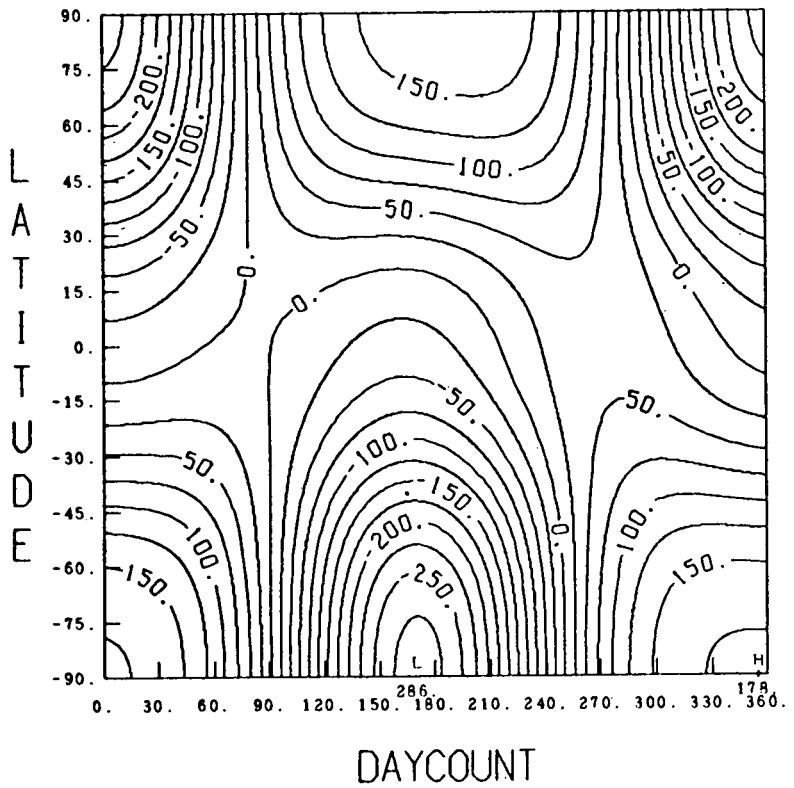

Figure 9g. Contour plot of departures of inferred exospheric temperature from the global mean (1098°K) using all annual and semiannual components (assuming an $F_{10.7}$ of 150).

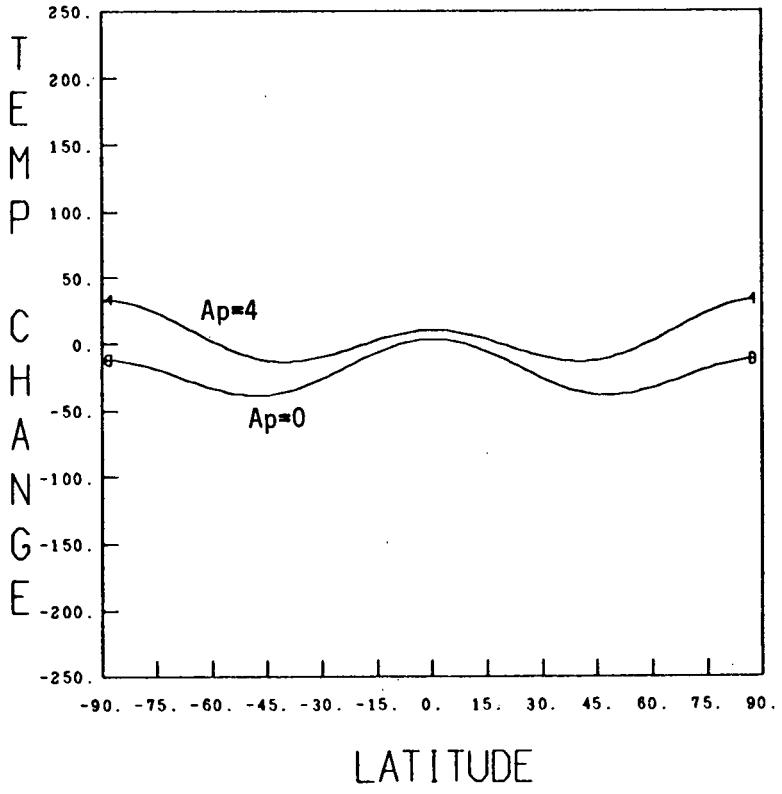

Figure 9h. Plot of temperature departures from the global mean versus geographic latitude using the time independent and magnetic activity components only.

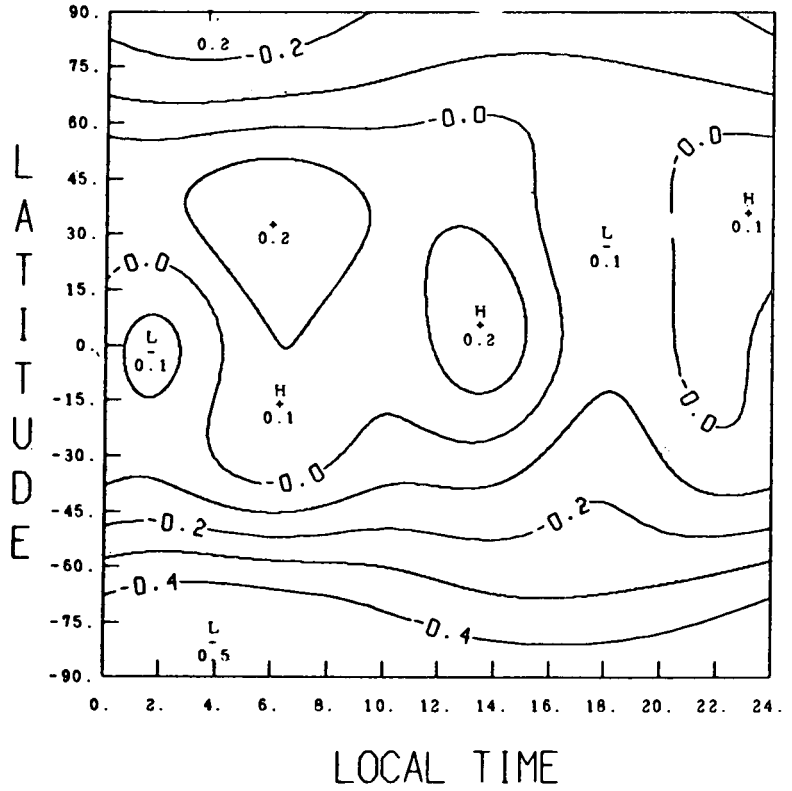

Figure 10a. Contour plot of the logarithm (base e) of the ratio of the inferred 120 km atomic oxygen densities to the global mean (8.97×10^{10} cm^{-3}) for September equinox conditions assuming an $F_{10.7}$ of 150 and an A_p of 4.

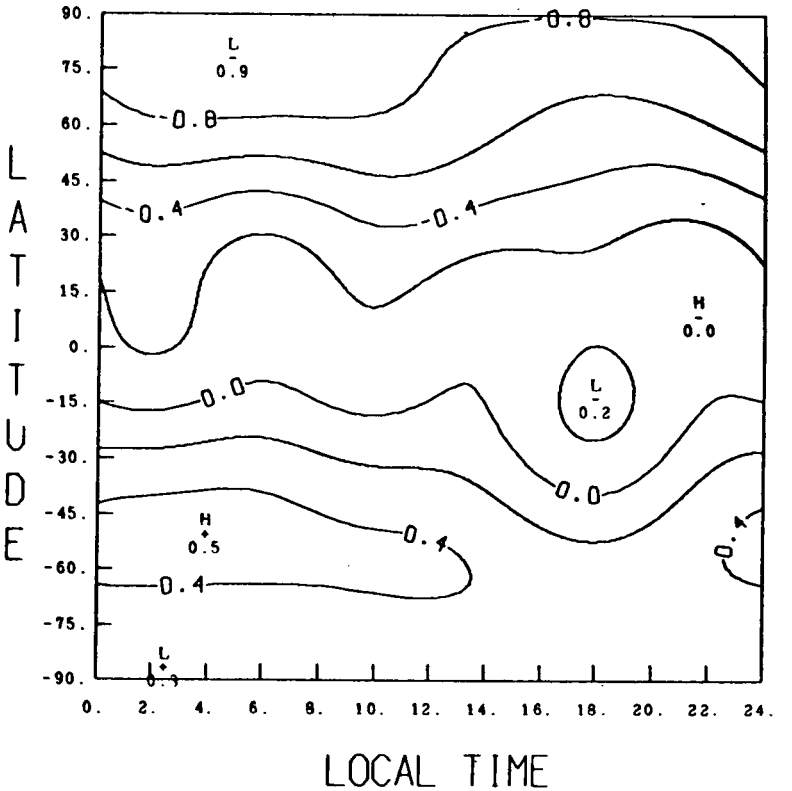

Figure 10b. Same as 10a for June solstice conditions.

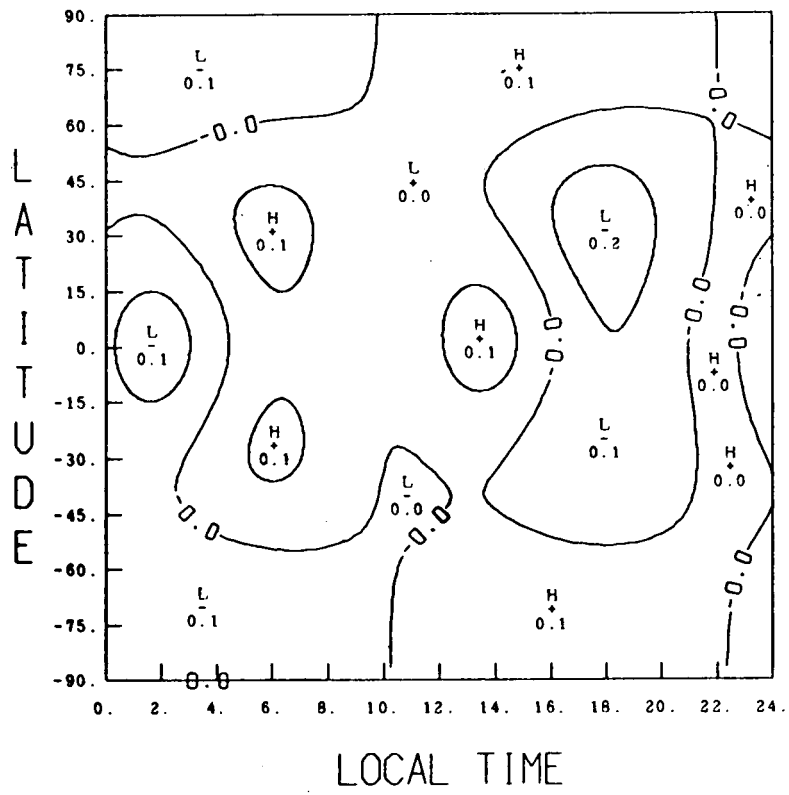

Figure 10c. Contour plot of the logarithm (base e) of the ratio of the inferred 120 km atomic oxygen densities to the global mean (8.97×10^{10} cm^{-3}) using the diurnal, semidiurnal, and terdiurnal components only for September equinox conditions (assuming an $F_{10.7}$ of 150).

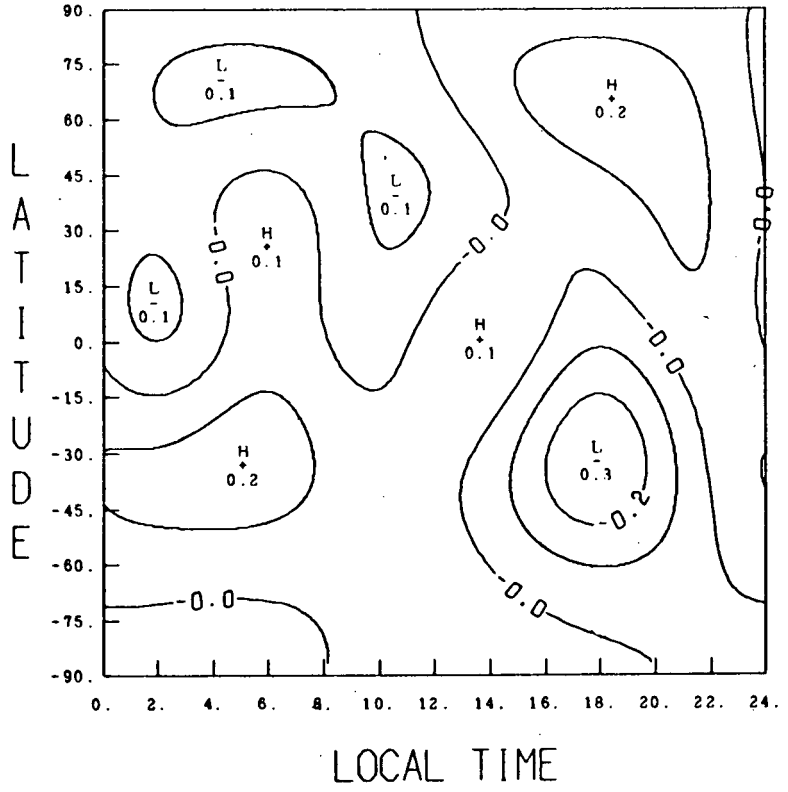

Figure 10d. Same as 10c for June solstice conditions.

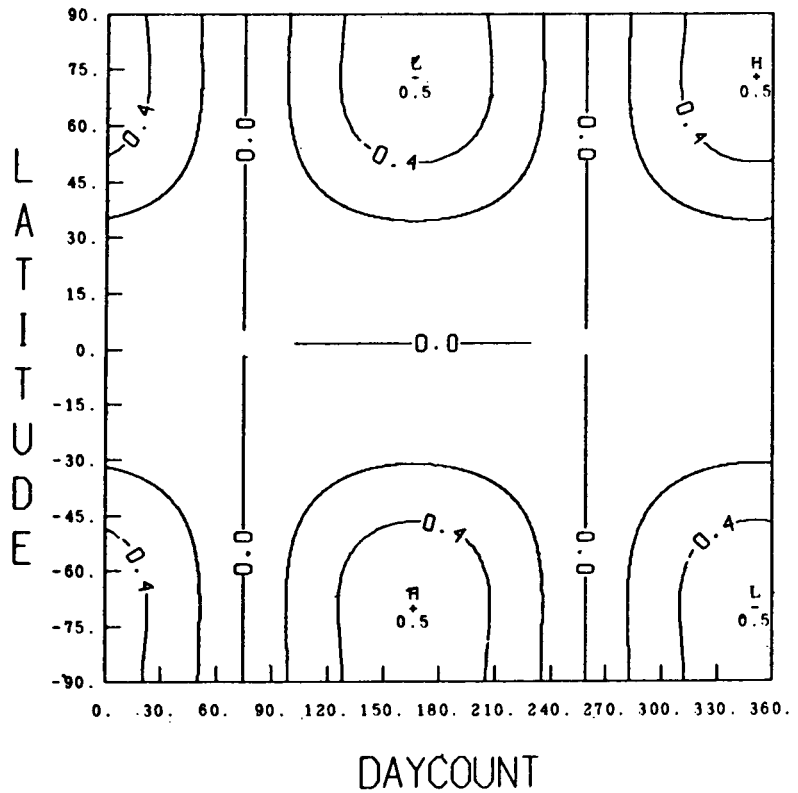

Figure 10e. Contour plot of the logarithm (base e) of the ratio of the inferred 120 km atomic oxygen densities to the global mean (8.97×10^{10} cm^{-3}) using the asymmetrical annual component only (assuming an $F_{10.7}$ of 150).

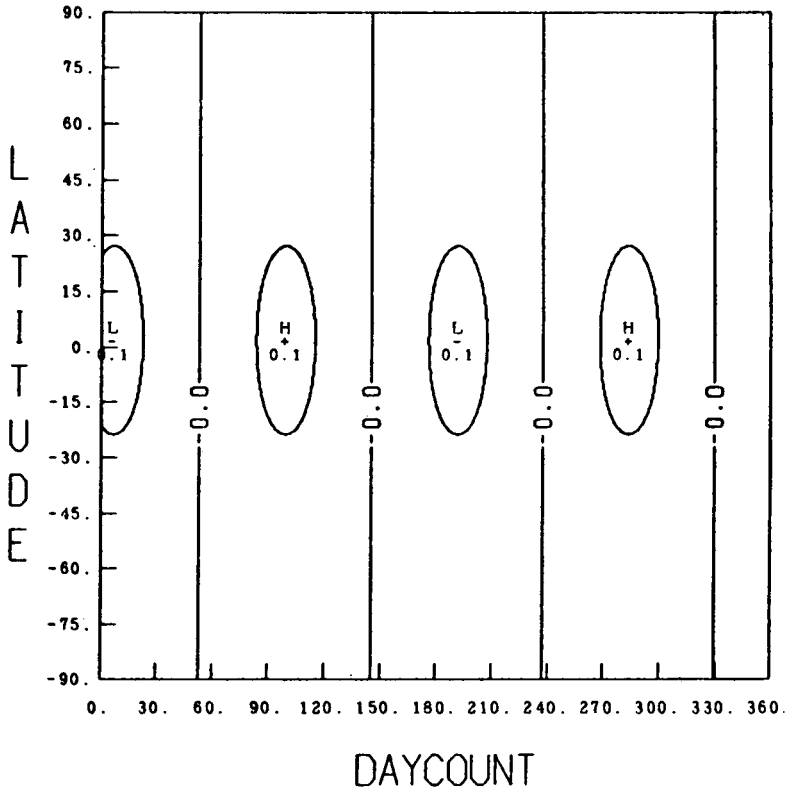

Figure 10f. Same as 10e using the symmetrical semiannual component only.

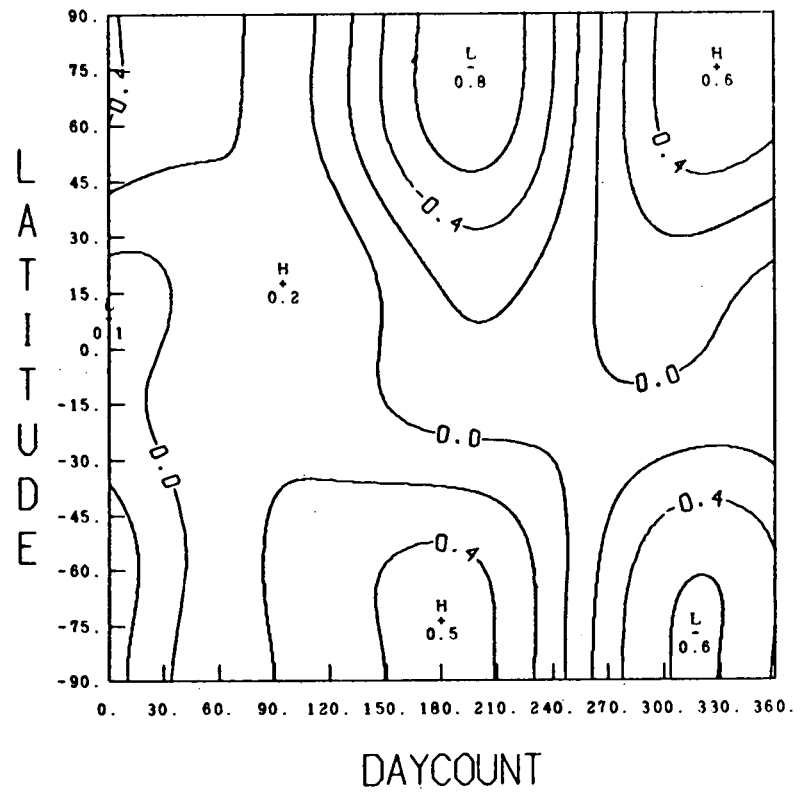

Figure 10g. Contour plot of the logarithm (base e) of the ratio of inferred 120 km atomic oxygen densities to the global mean (8.97×10^{10} cm^{-3}) using all annual and semiannual components (assuming an $F_{10.7}$ of 150).

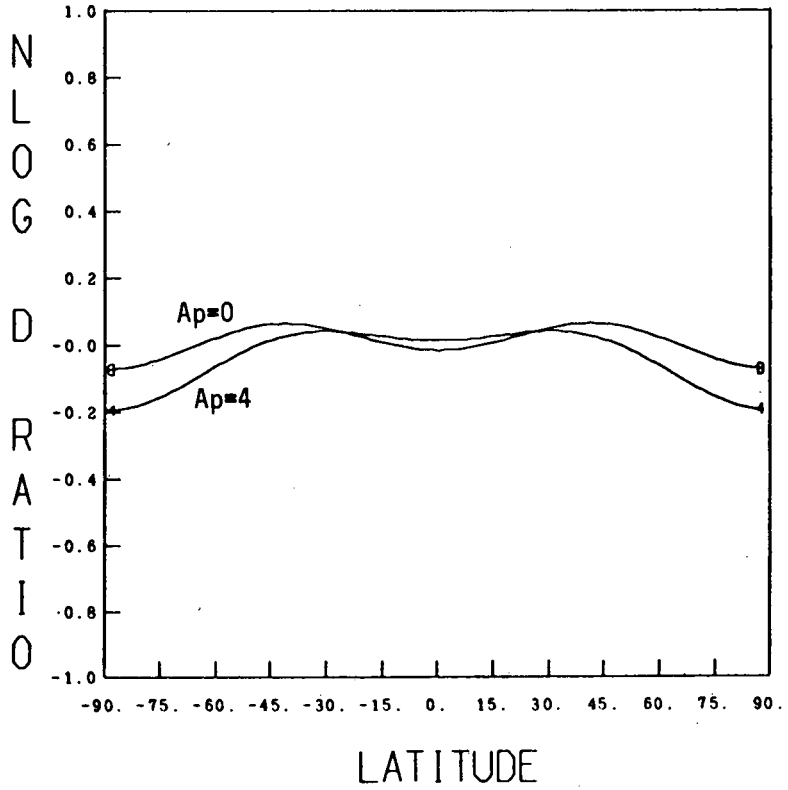

Figure 10h. Plot of the logarithm (base e) of the ratio of the inferred 120 km atomic oxygen densities to the global mean versus geographic latitude using the time dependent and magnetic activity components only.

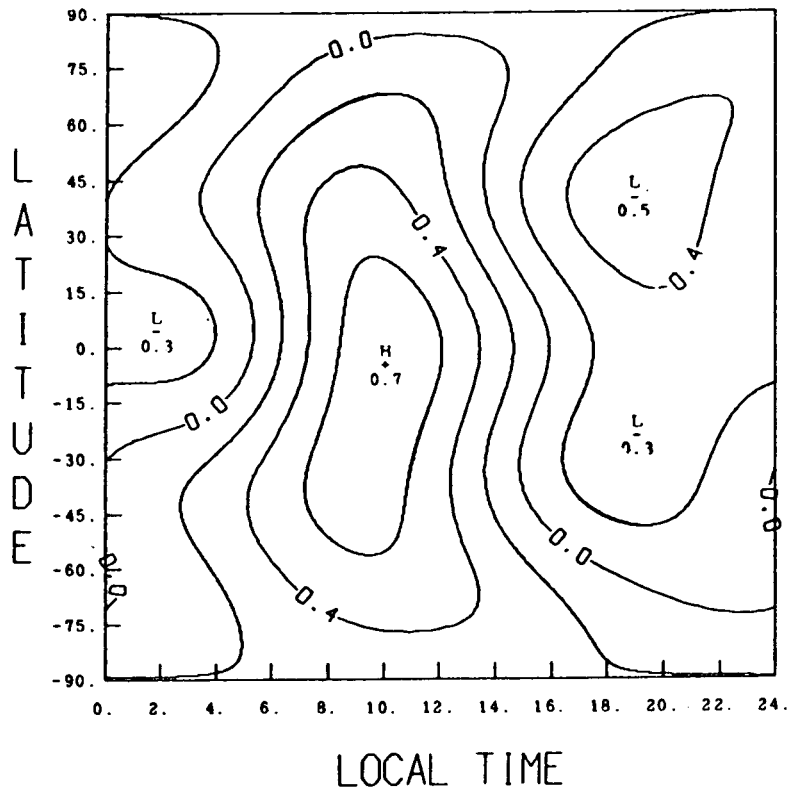

Figure 11a. Contour plot of the logarithm (base e) of the ratio of the inferred 120 km helium densities to the global mean (2.73×10^7 cm^{-3}) for September equinox conditions assuming an $F_{10.7}$ of 150 and an A_p of 4.

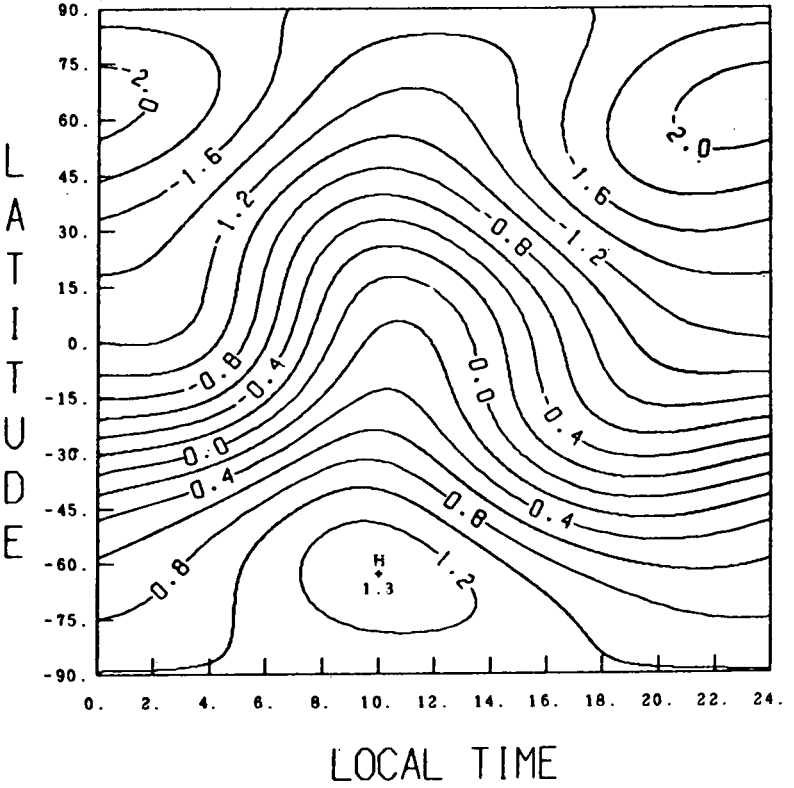

Figure 11b. Same as 11a for June solstice conditions.

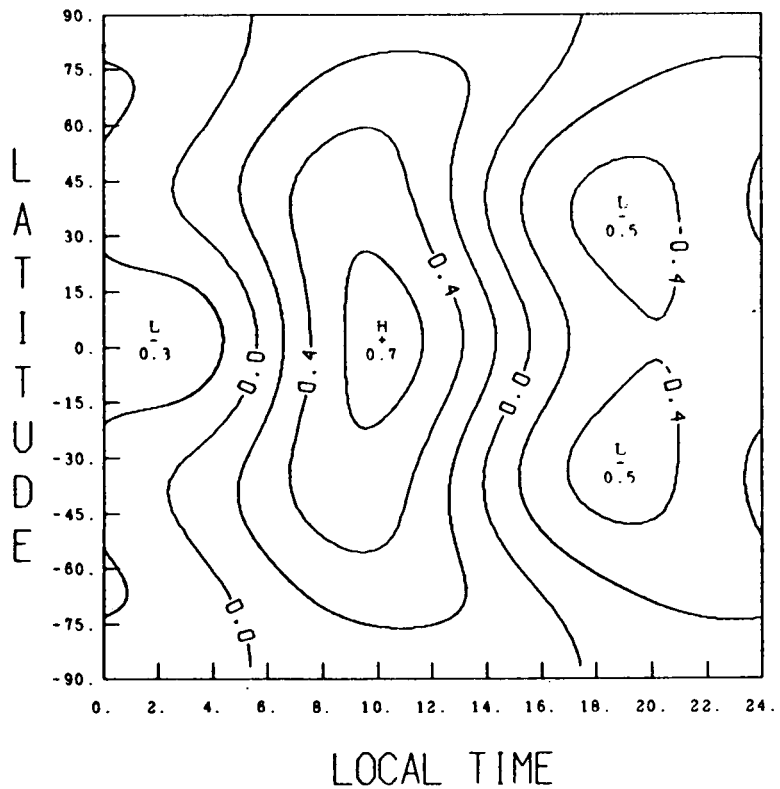

Figure 11c. Contour plot of the logarithm (base e) of the ratio of the inferred 120 km helium densities to the global mean (2.73×10^7 cm^{-3}) using the diurnal, semi-diurnal, and terdiurnal components only for September equinox conditions (assuming an $F_{10.7}$ of 150).

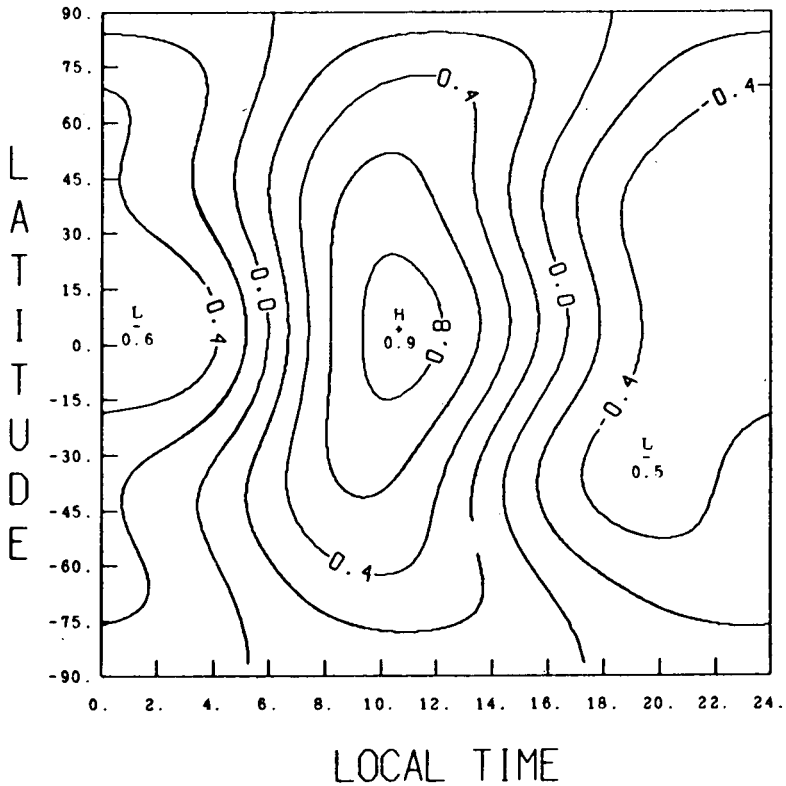

Figure 11d. Same as 11c for June solstice conditions.

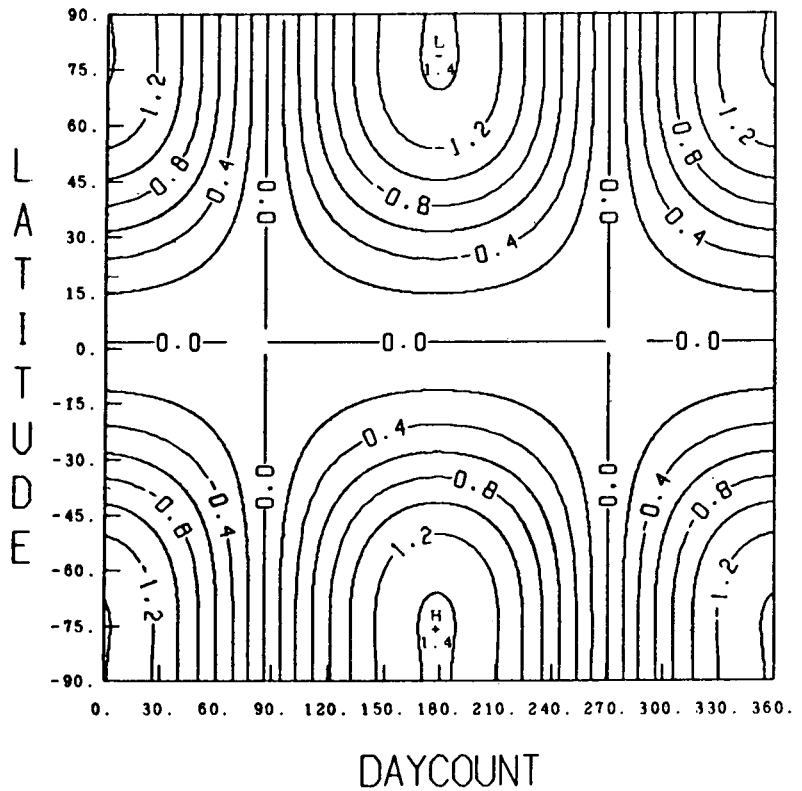

Figure 11e. Contour plot of the logarithm (base e) of the ratio of the inferred 120 km helium densities to the global mean (2.73×10^7 cm^{-3}) using the asymmetrical annual component only (assuming an $F_{10.7}$ of 150).

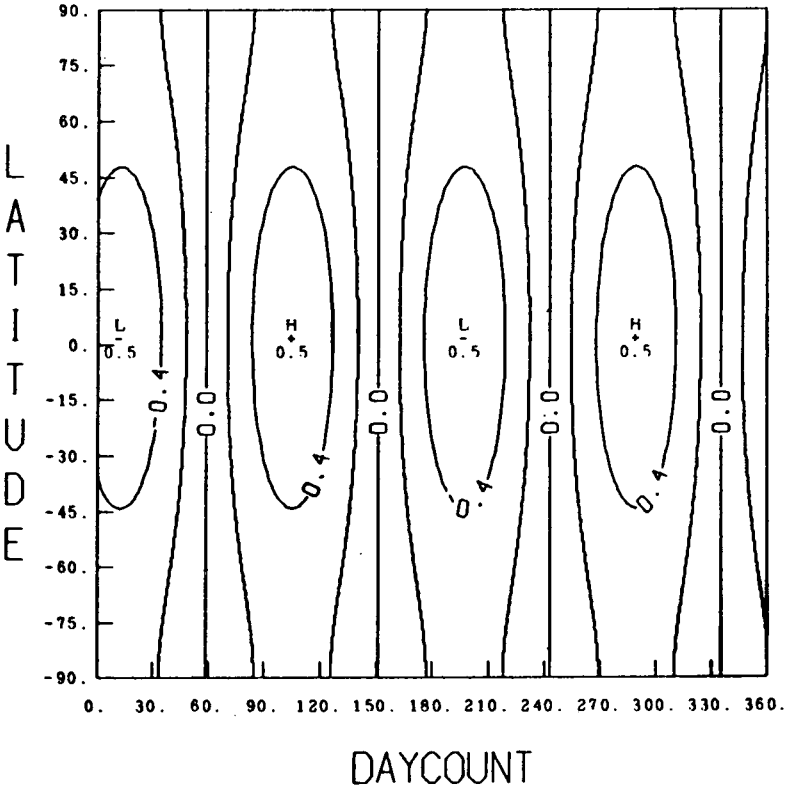

Figure 11f. Same as 11e using the symmetrical semiannual component only.

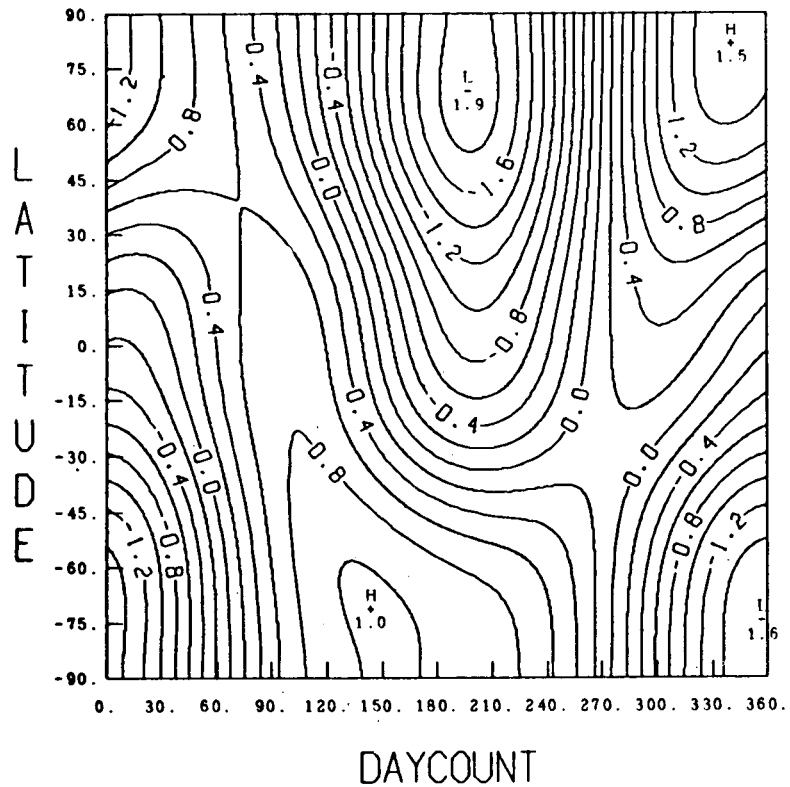

Figure 11g. Contour plot of the logarithm (base e) of the ratio of the inferred 120 km helium densities to the global mean (2.73×10^7 cm^{-3}) using all annual and semiannual components (assuming an $F_{10.7}$ of 150).

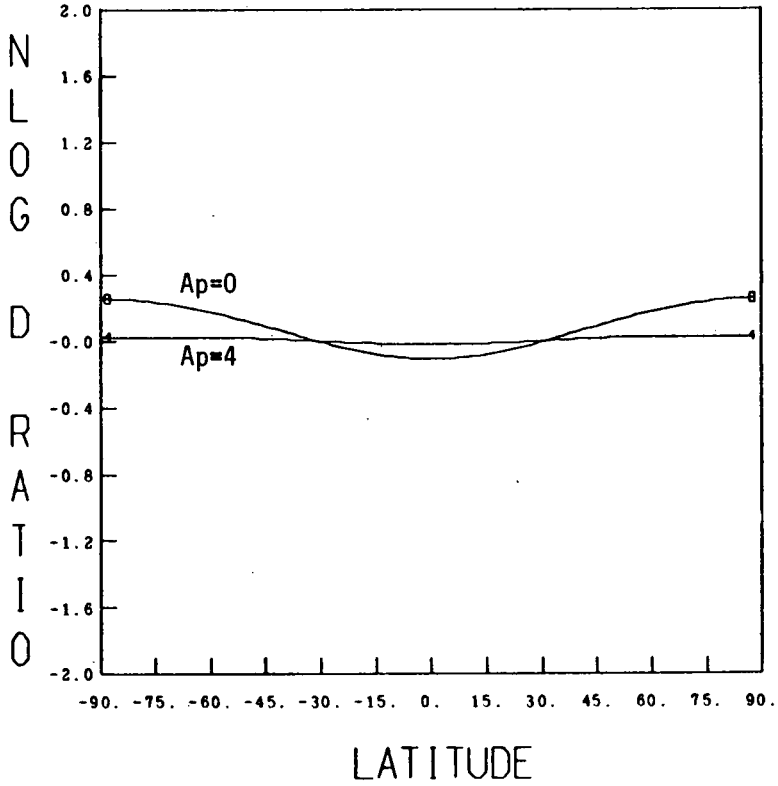

Figure 11h. Plot of the logarithm (base e) of the ratio of the inferred 120 km helium densities to the global mean versus geographic latitude using the time independent and magnetic activity components only.

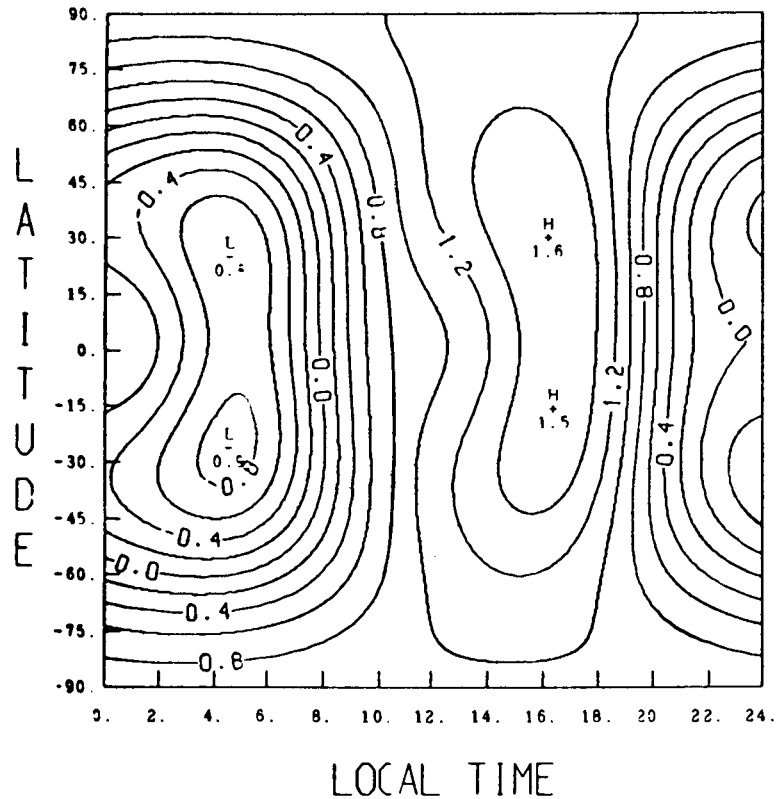

Figure 12a. Contour plot of the logarithm (base e) of the ratio of the inferred 450 km nitrogen densities to the global mean (2.16×10^6 cm^{-3}) for September equinox conditions assuming an $F_{10.7}$ of 150 and an A_p of 4.

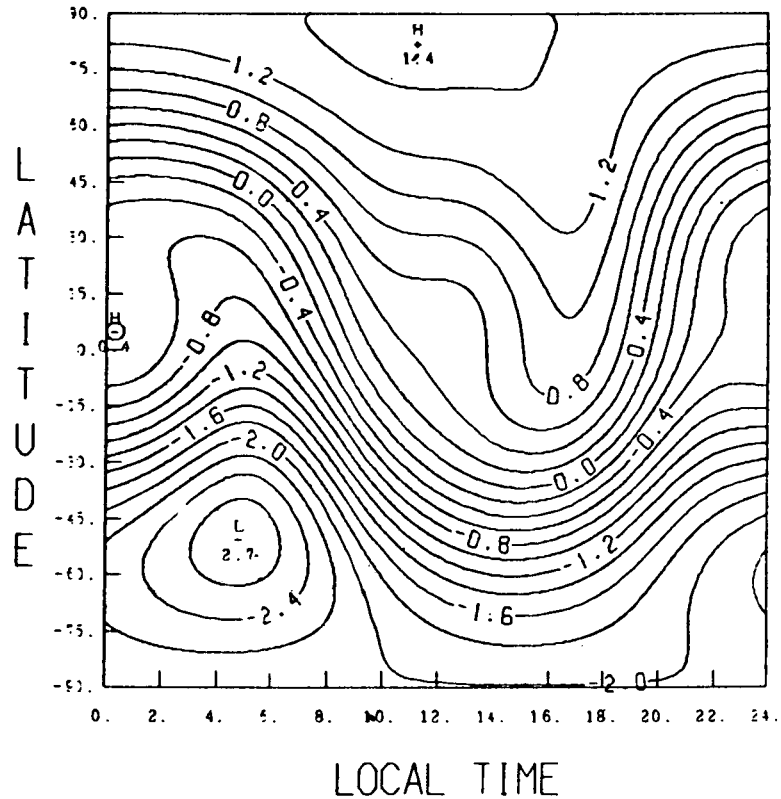

Figure 12b. Same as 12a for June solstice conditions.

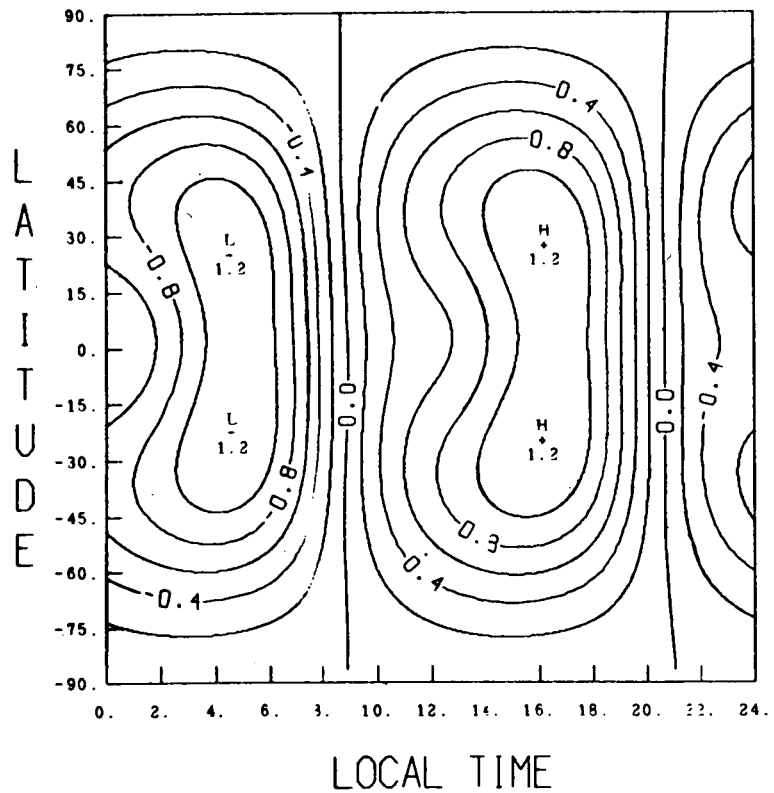

Figure 12c. Contour plot of the logarithm (base e) of the ratio of the 450 km nitrogen densities to the global mean (2.16×10^6 cm^{-3}) using the diurnal, semi-diurnal, and terdiurnal components only for September equinox conditions (assuming an $F_{10.7}$ of 150).

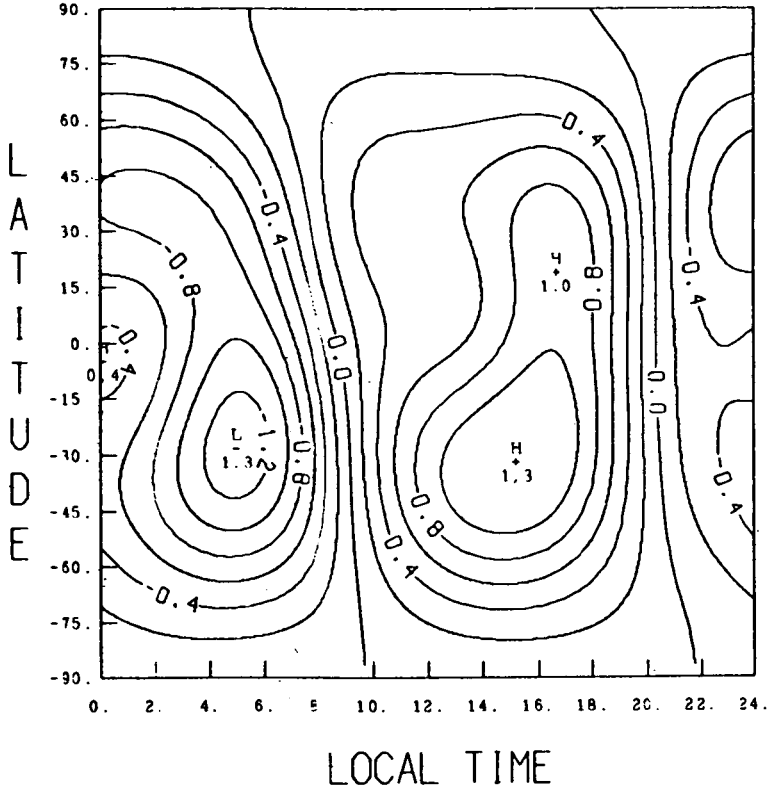

Figure 12d. Same as 12c for June solstice conditions.

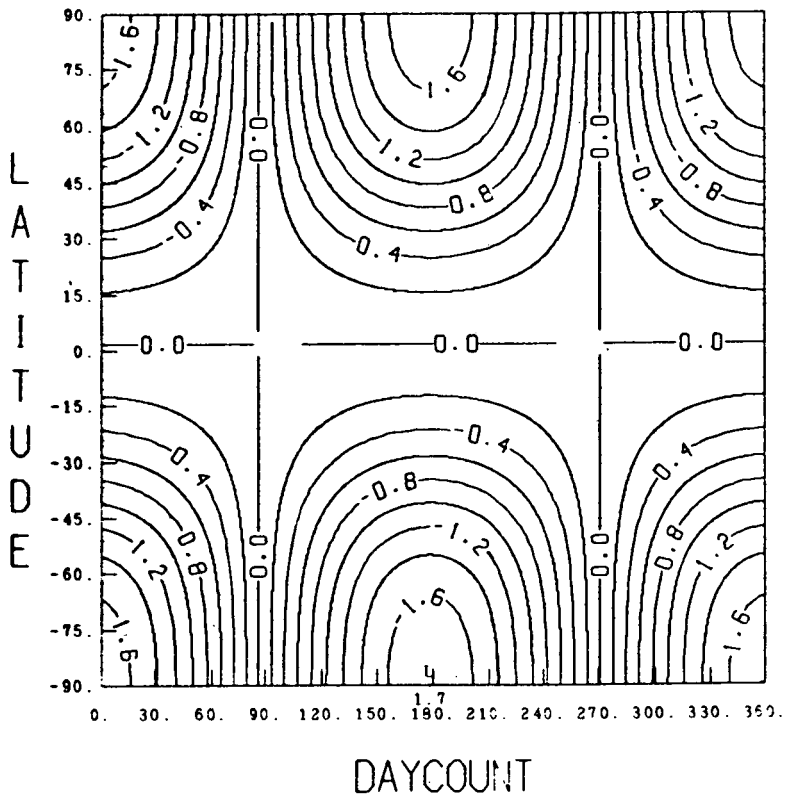

Figure 12e. Contour plot of the logarithm (base e) of the ratio of 450 km nitrogen densities to the global mean (2.16×10^6 cm^{-3}) using the asymmetrical annual component only (assuming an $F_{10.7}$ of 150).

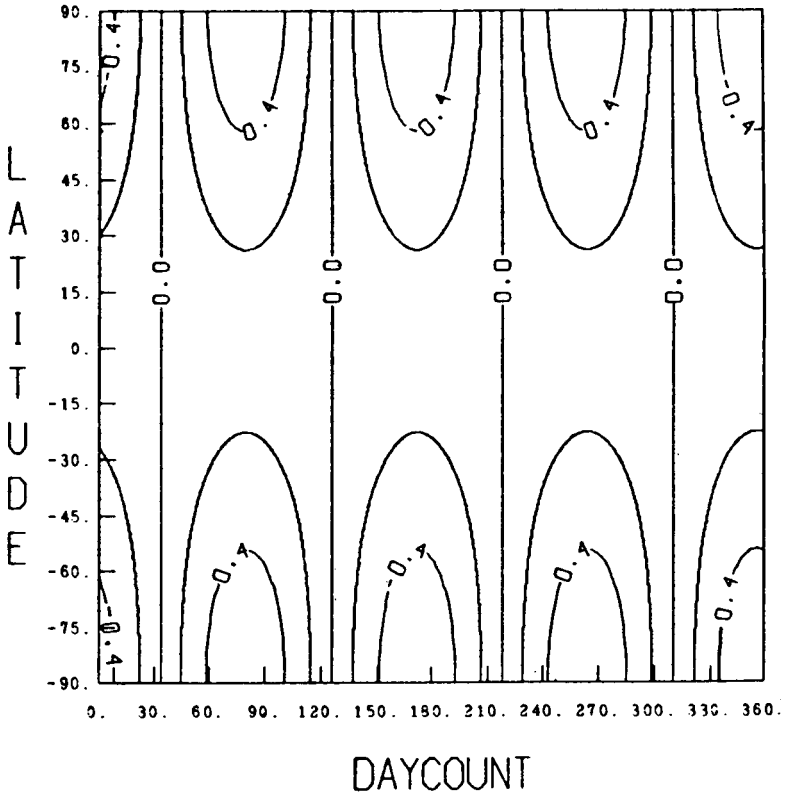

Figure 12f. Same as 12e using the symmetrical semiannual component only.

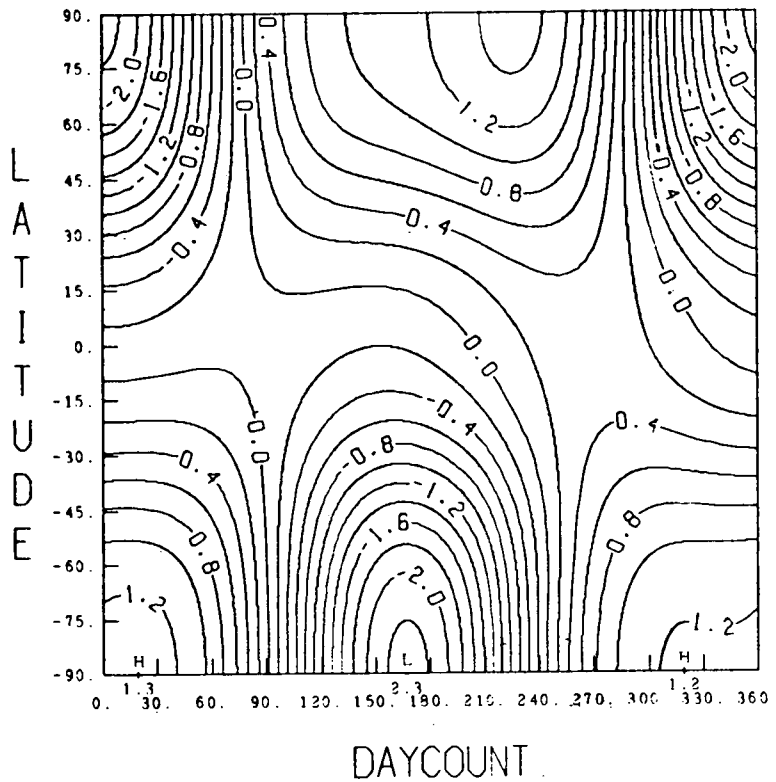

Figure 12g. Contour plot of the logarithm (base e) of the ratio of 450 km nitrogen densities to the global mean (2.16×10^6 cm^{-3}) using all annual and semiannual components (assuming an $F_{10.7}$ of 150).

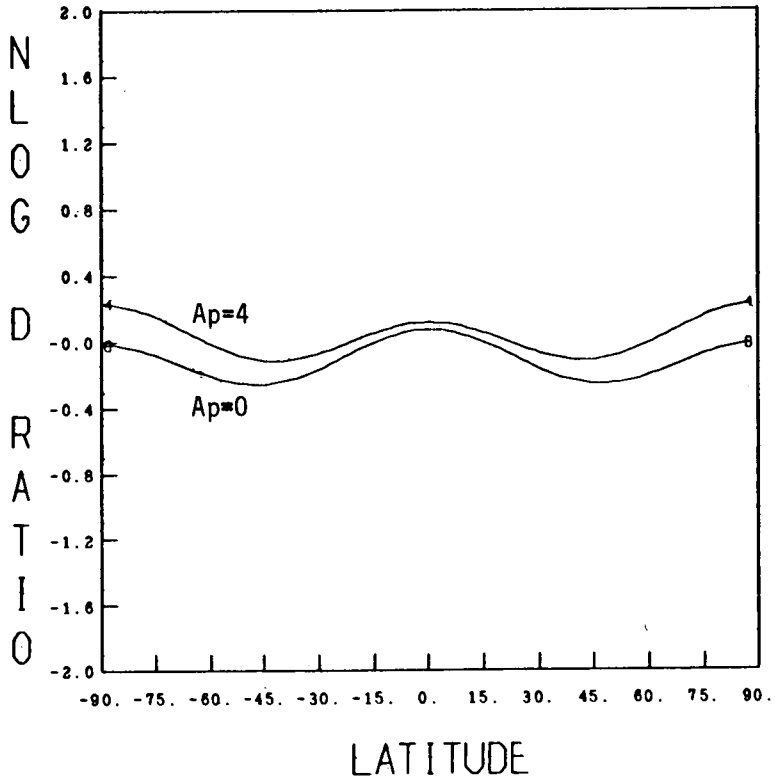

Figure 12h. Plot of the logarithm (base e) of the ratio of the 450 km nitrogen densities to the global mean versus geographic latitude using the time independent and magnetic activity components only.

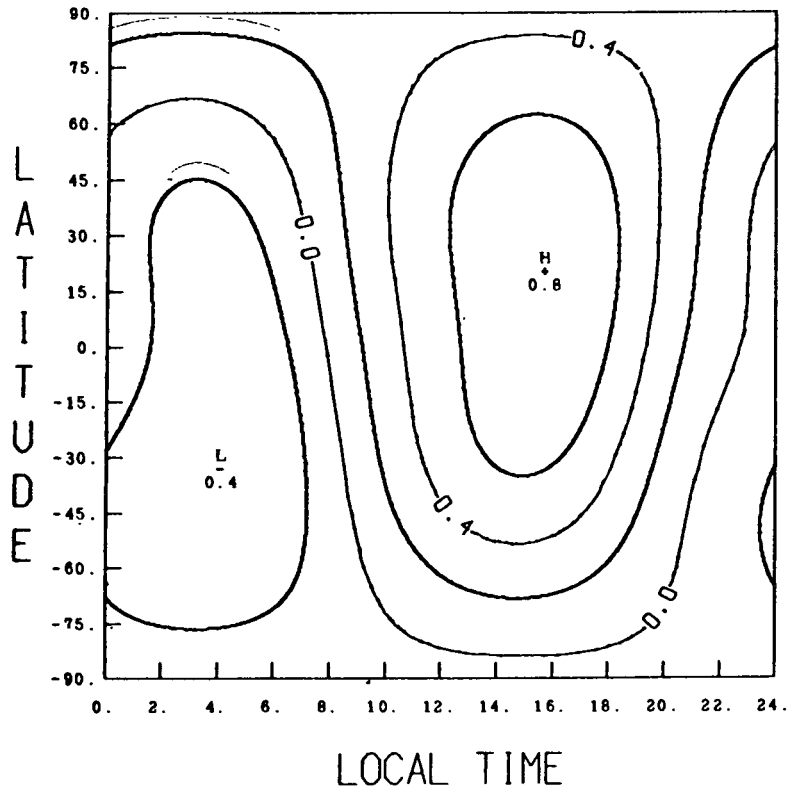

Figure 13a. Contour plot of the logarithm (base e) of the ratio of the 450 km atomic oxygen densities to the global mean (6.72×10^7 cm^{-3}) for September equinox conditions assuming an $F_{10.7}$ of 150 and an A_p of 4.

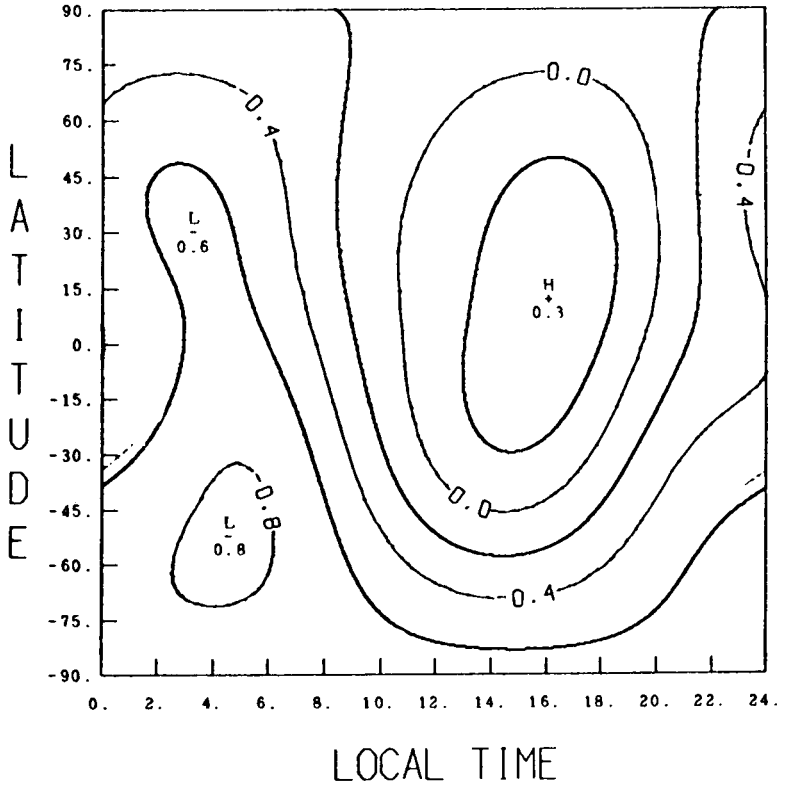

Figure 13b. Same as 13a for June solstice conditions.

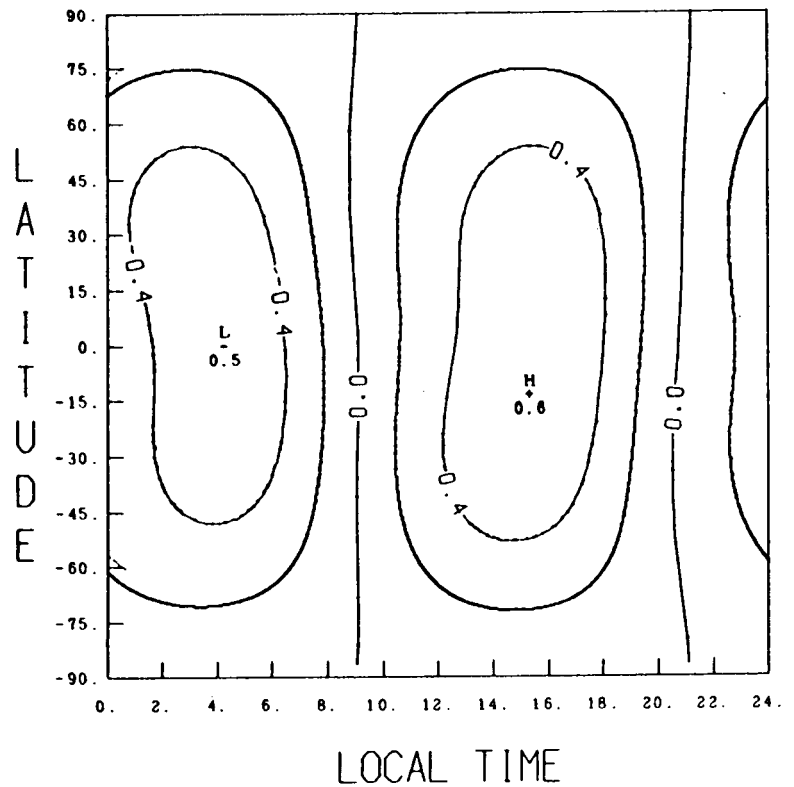

Figure 13c. Contour plot of the logarithm (base e) of the ratio of the 450 km atomic oxygen densities to the global mean (6.72×10^7 cm^{-3}) using the diurnal, semi-diurnal, and terdiurnal components only for September equinox conditions (assuming an $F_{10.7}$ of 150).

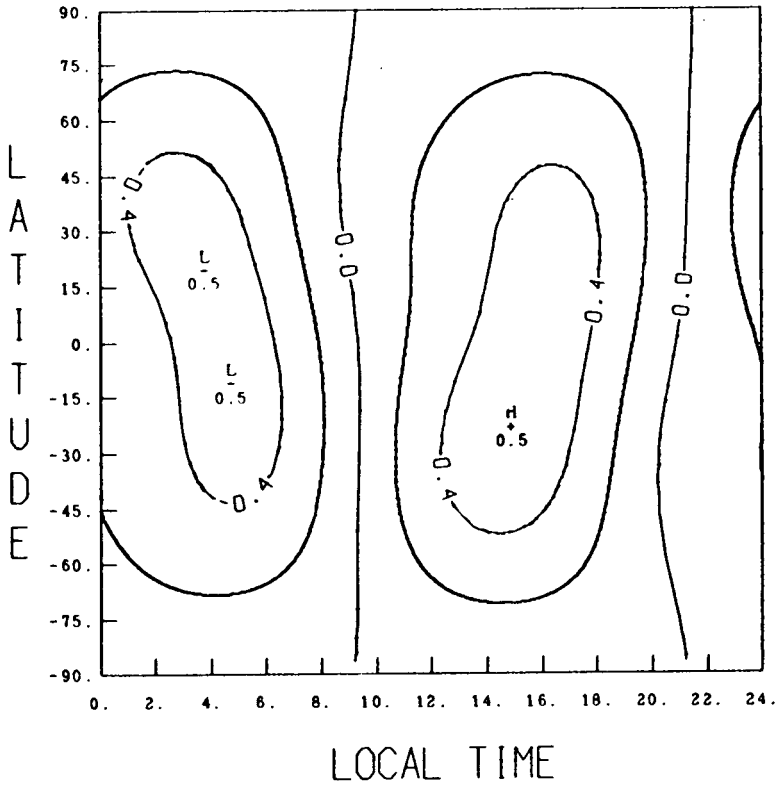

Figure 13d. Same as 13c for June solstice conditions.

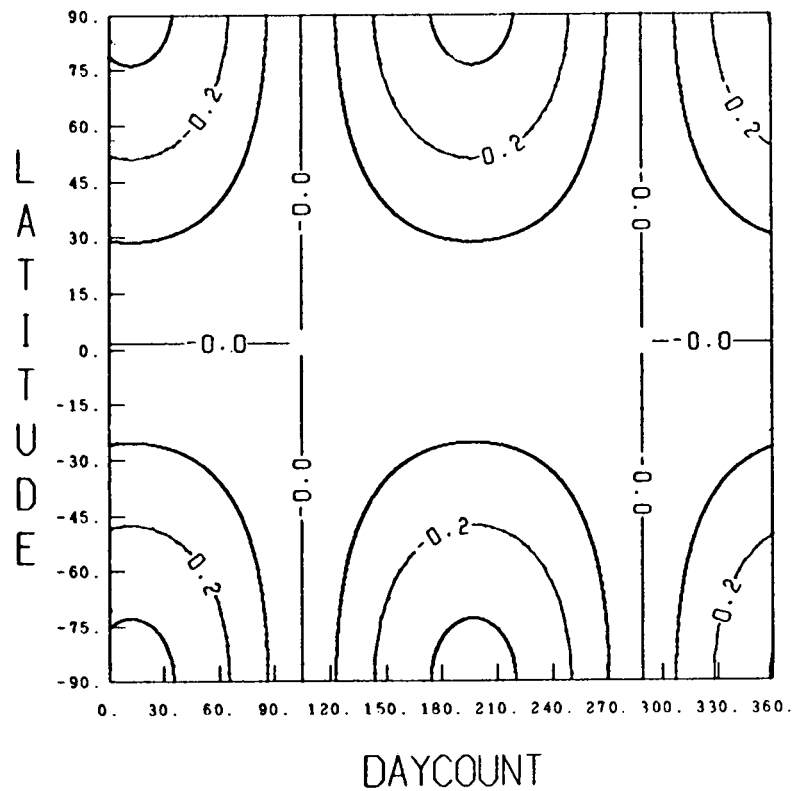

Figure 13e. Contour plot of the logarithm (base e) of the ratio of the 450 km atomic oxygen densities to the global mean (6.72×10^7 cm^{-3}) using the asymmetrical annual component only (assuming an $F_{10.7}$ of 150).

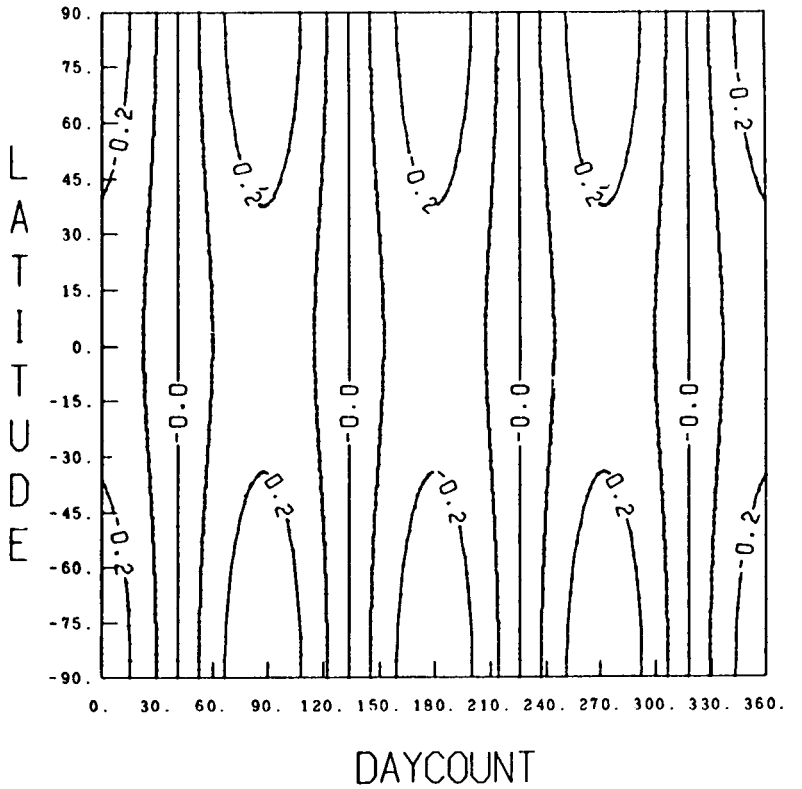

Figure 13f. Same as 13e using the symmetrical semiannual component only.

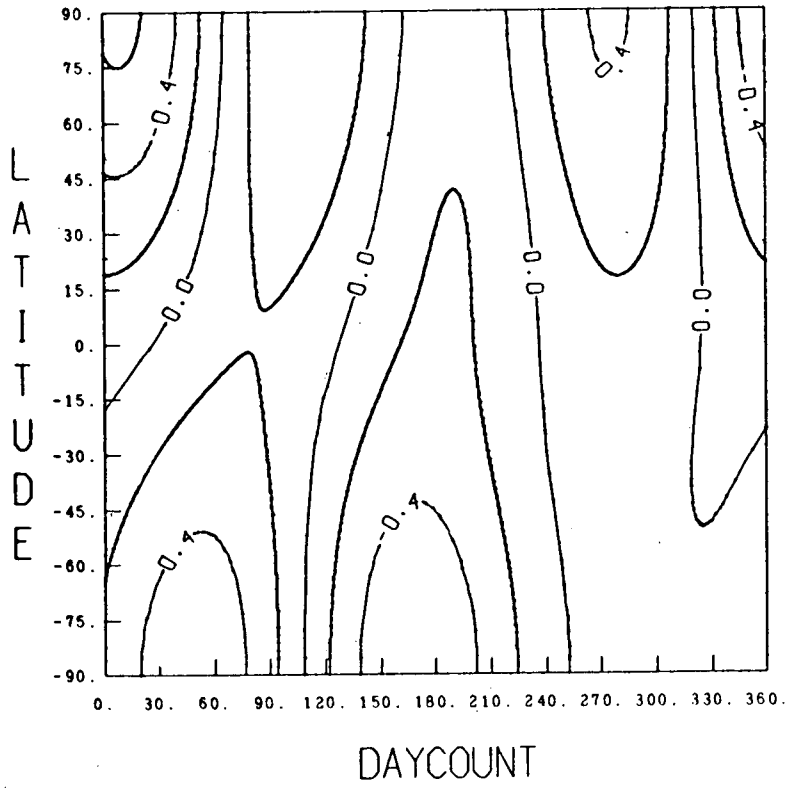

Figure 13g. Contour plot of the logarithm (base e) of the ratio of the 450 km atomic oxygen densities to the global mean (6.72×10^7 cm^{-3}) using all annual and semi-annual components (assuming an $F_{10.7}$ of 150).

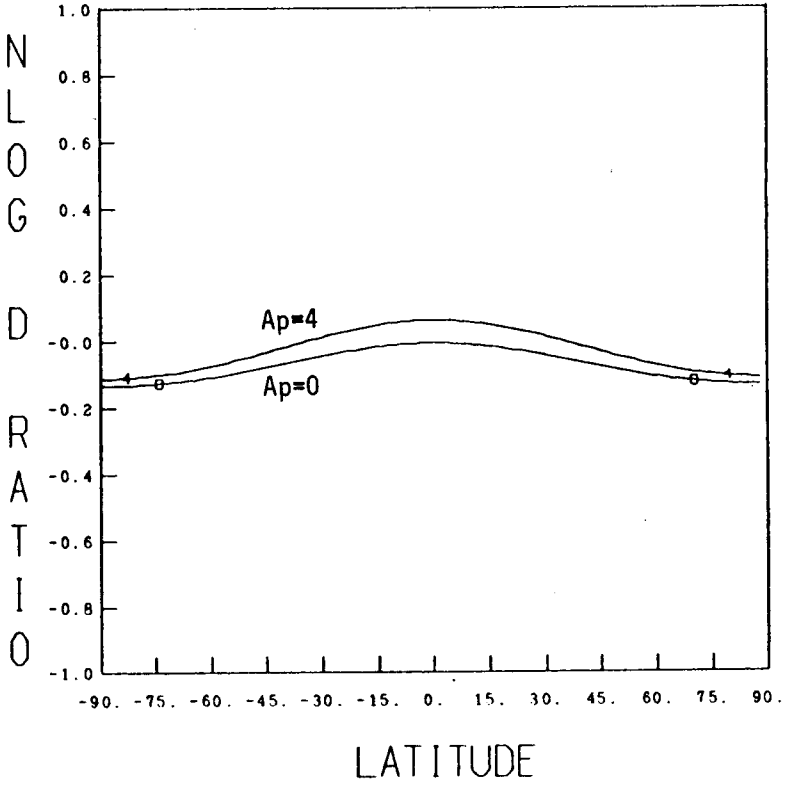

Figure 13h. Plot of the logarithm (base e) of the ratio of the 450 km atomic oxygen densities to the global mean versus geographic latitude using the time independent and magnetic activity components only.

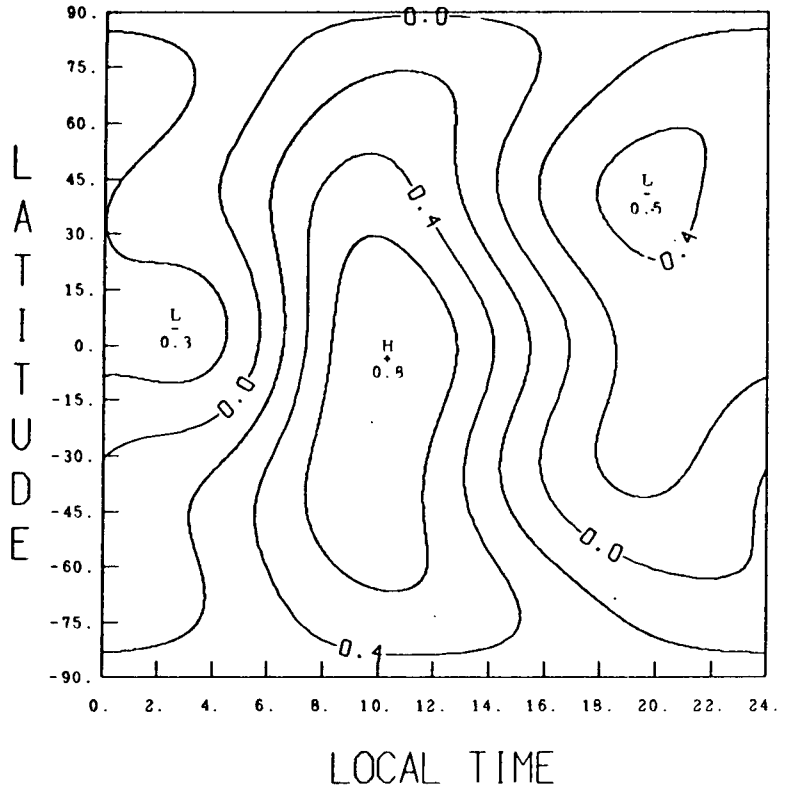

Figure 14a. Contour plot of the logarithm (base e) of the ratio of the 450 km helium densities to the global mean (3.02×10^6 cm^{-3}) for September equinox conditions assuming an $F_{10.7}$ of 150 and an A_p of 4.

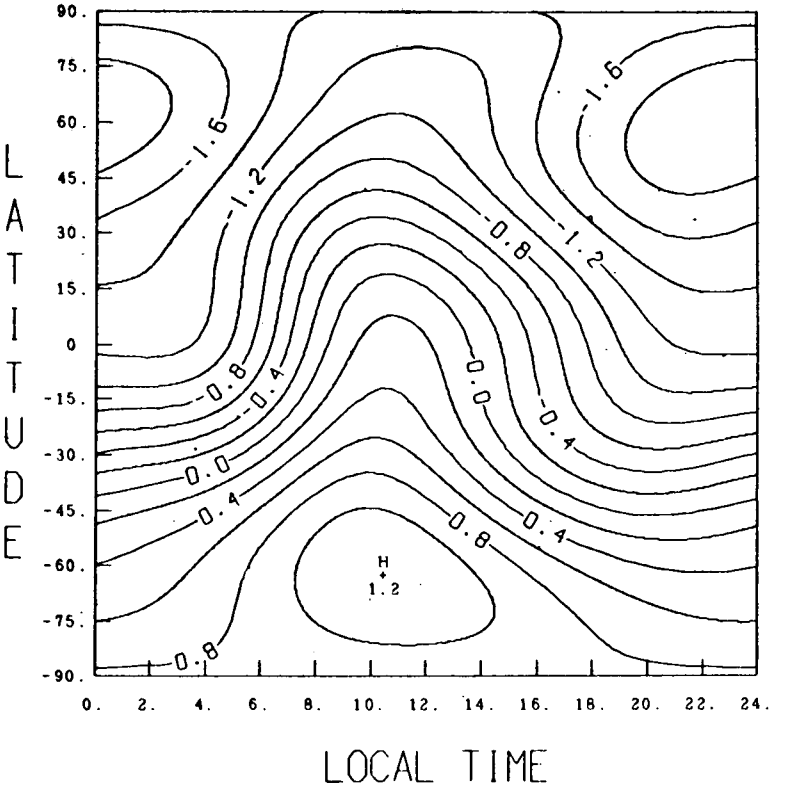

Figure 14b. Same as 14a for June solstice conditions.

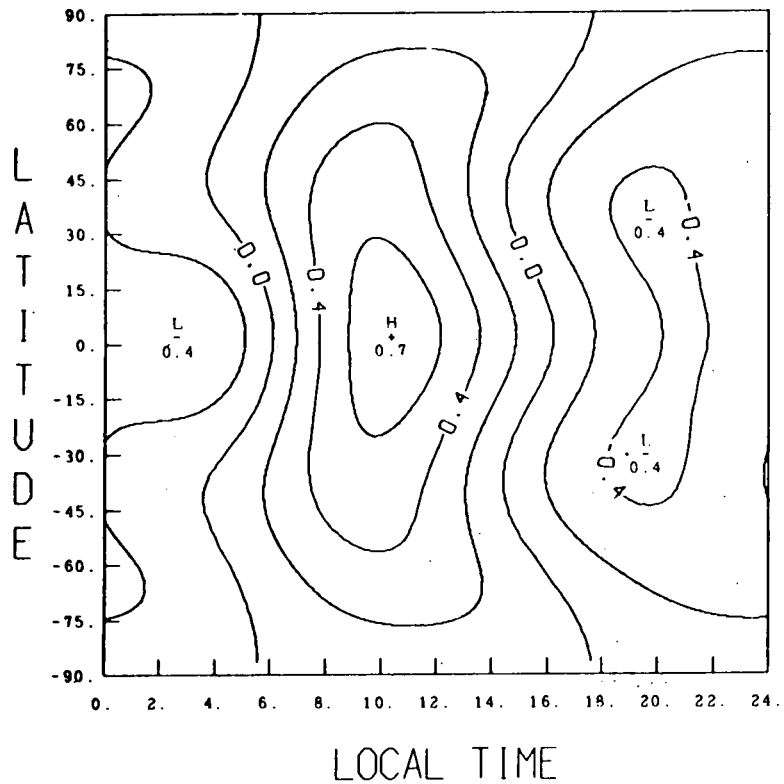

Figure 14c. Contour plot of the logarithm (base e) of the ratio of the 450 km helium densities to the global mean (3.02×10^6 cm^{-3}) using the diurnal, semidiurnal, and terdiurnal components only for September equinox conditions (assuming an $F_{10.7}$ of 150).

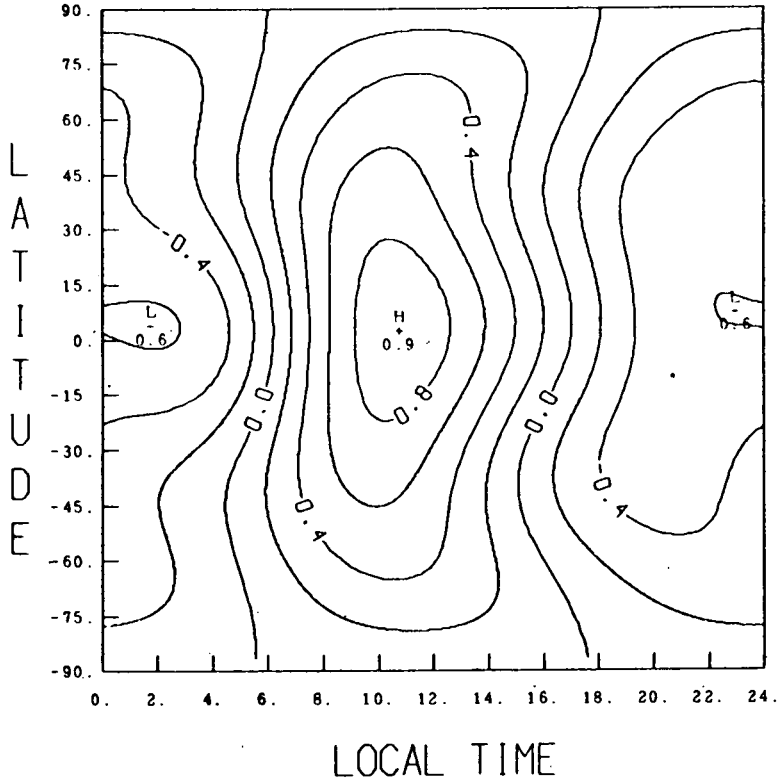

Figure 14d. Same as 14c for June solstice conditions.

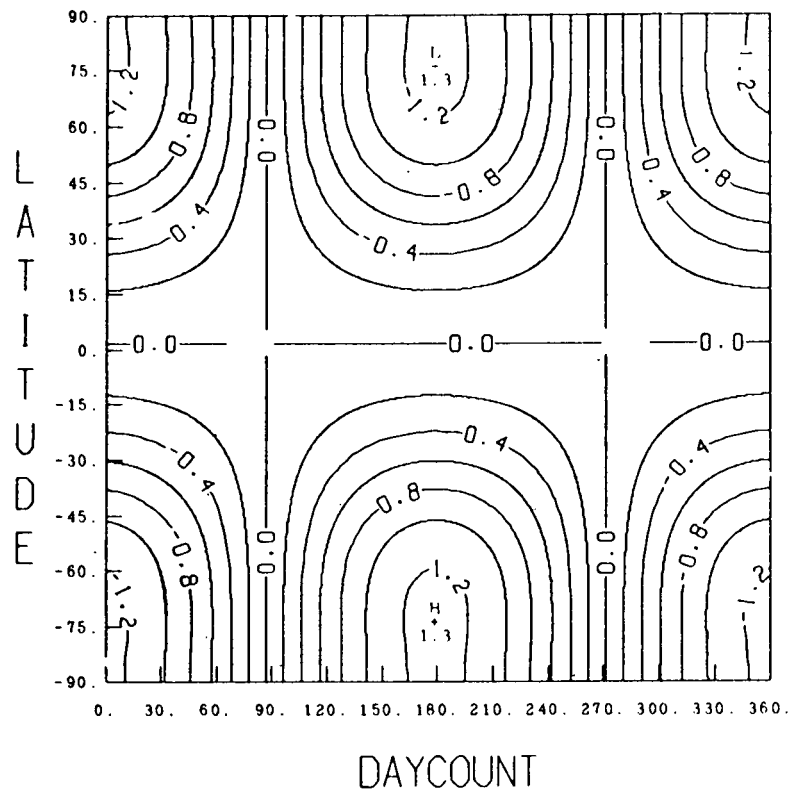

Figure 14e. Contour plot of the logarithm (base e) of the ratio of the 450 km helium densities to the global mean (3.02×10^6 cm^{-3}) using the asymmetrical annual component only (assuming an $F_{10.7}$ of 150).

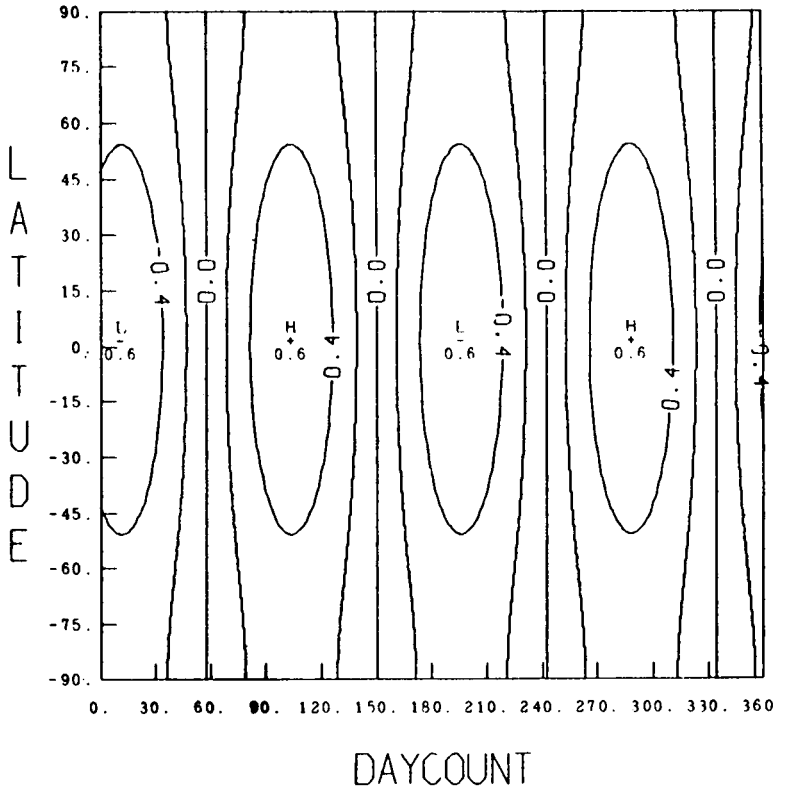

Figure 14f. Same as 14e using the symmetrical semiannual component only.

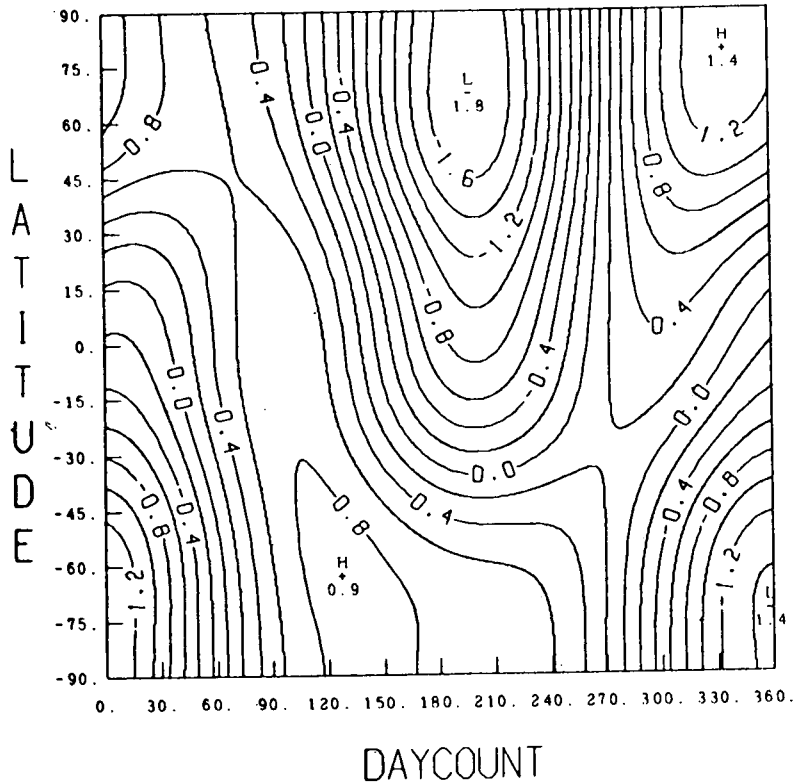

Figure 14g. Contour plot of the logarithm (base e) of the ratio of the 450 km helium densities to the global mean (3.02×10^6 cm^{-3}) using all annual and semiannual components (assuming an $F_{10.7}$ of 150).

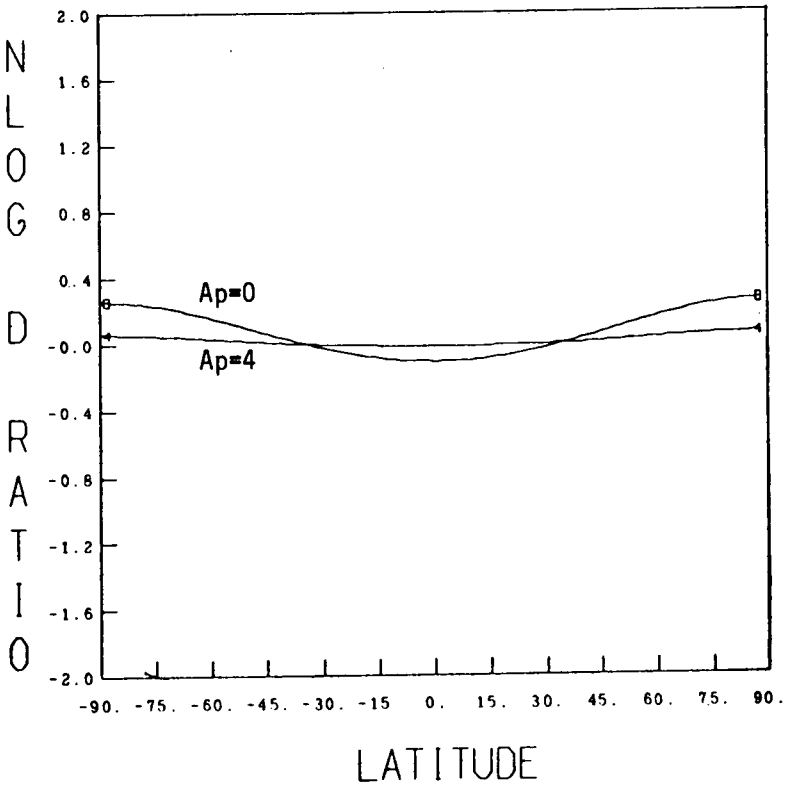

Figure 14h. Plot of the logarithm (base e) of the ratio of the 450 km helium densities to the global mean versus geographic latitude using the time independent and magnetic activity components only.

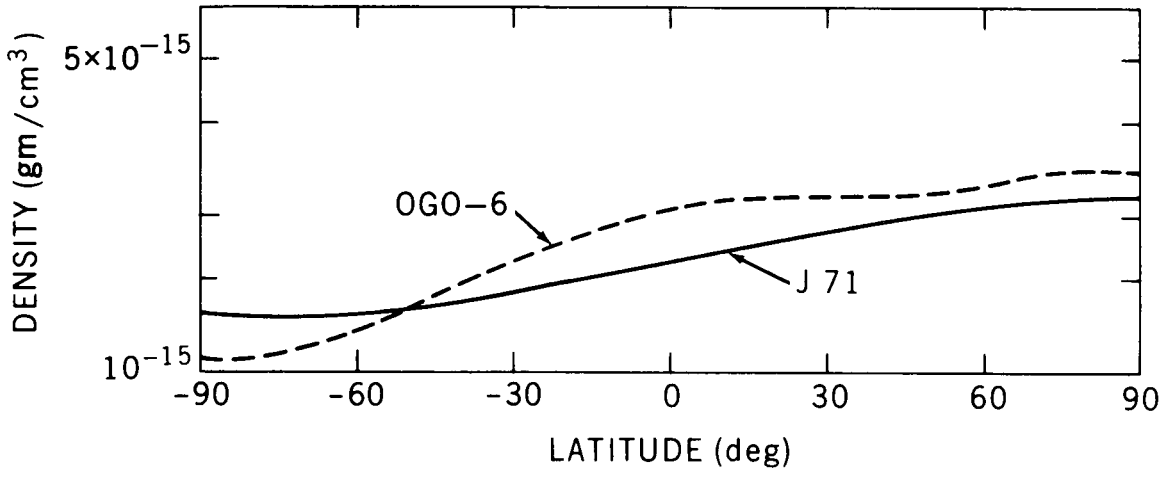

Figure 15a. Diurnally averaged total mass density at 450 km as a function of latitude for solstice conditions (summer at right) for the Jacchia Model (J71) and the OGO-6 empirical model.

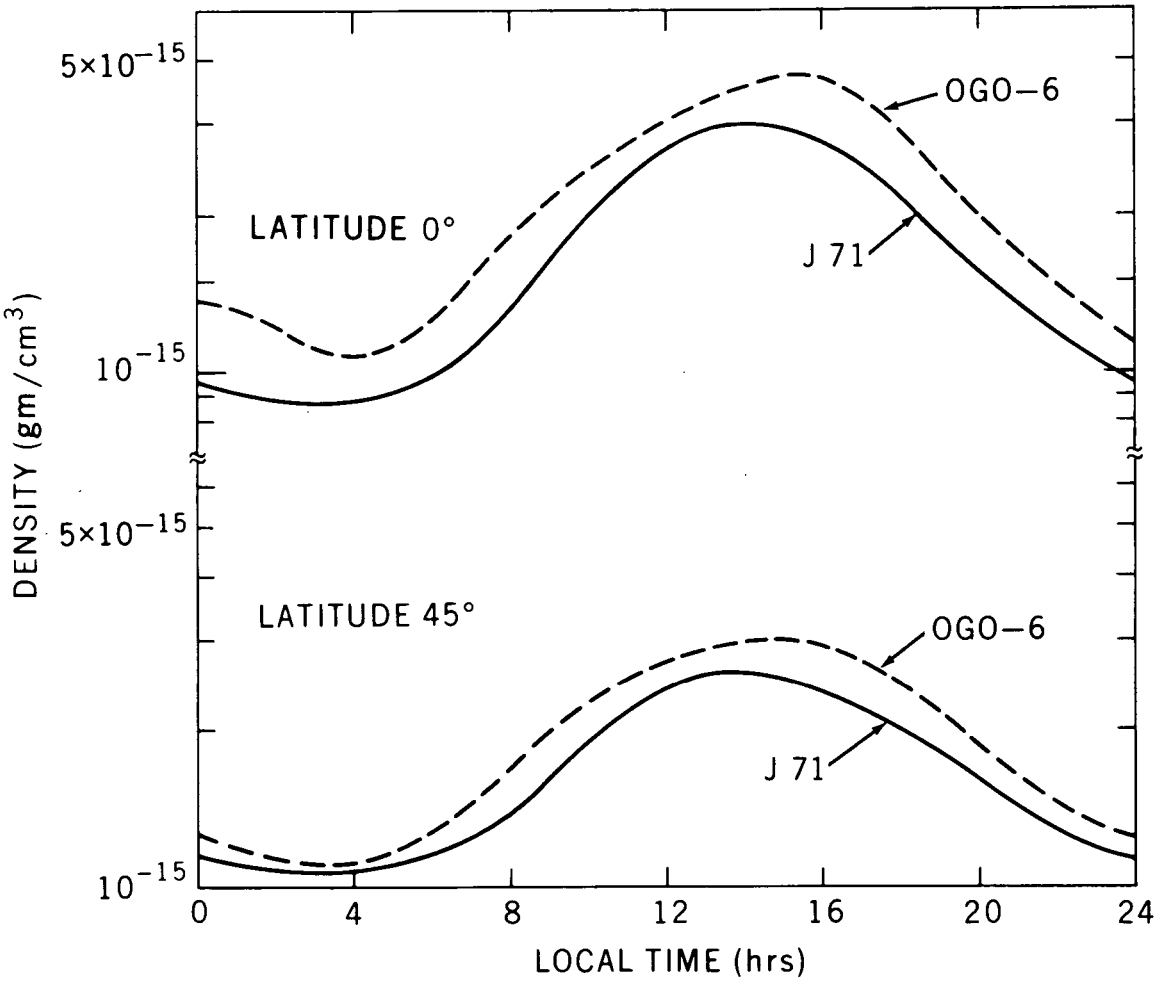

Figure 15b. Total mass density at 450 km as a function of local time at equinox for latitudes 0° and 45° for the Jacchia model (J71) and the OGO-6 empirical model.

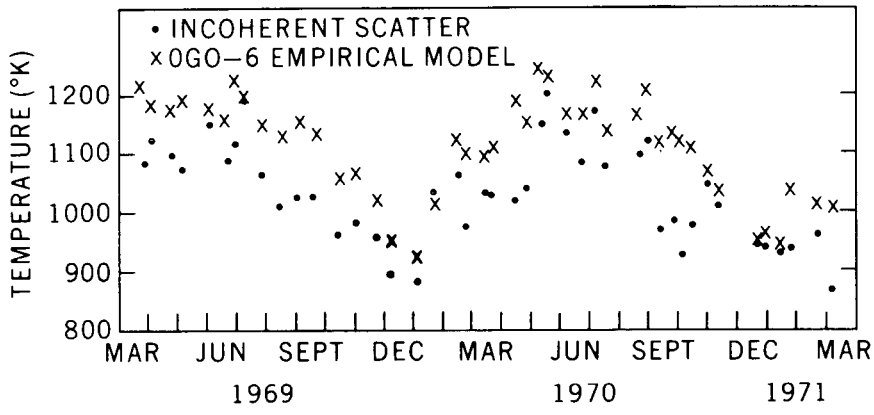

Figure 16a. Diurnally averaged exospheric temperature as a function of day for incoherent scatter measurements [Salah and Evans, 1972] and the OGO-6 empirical model.

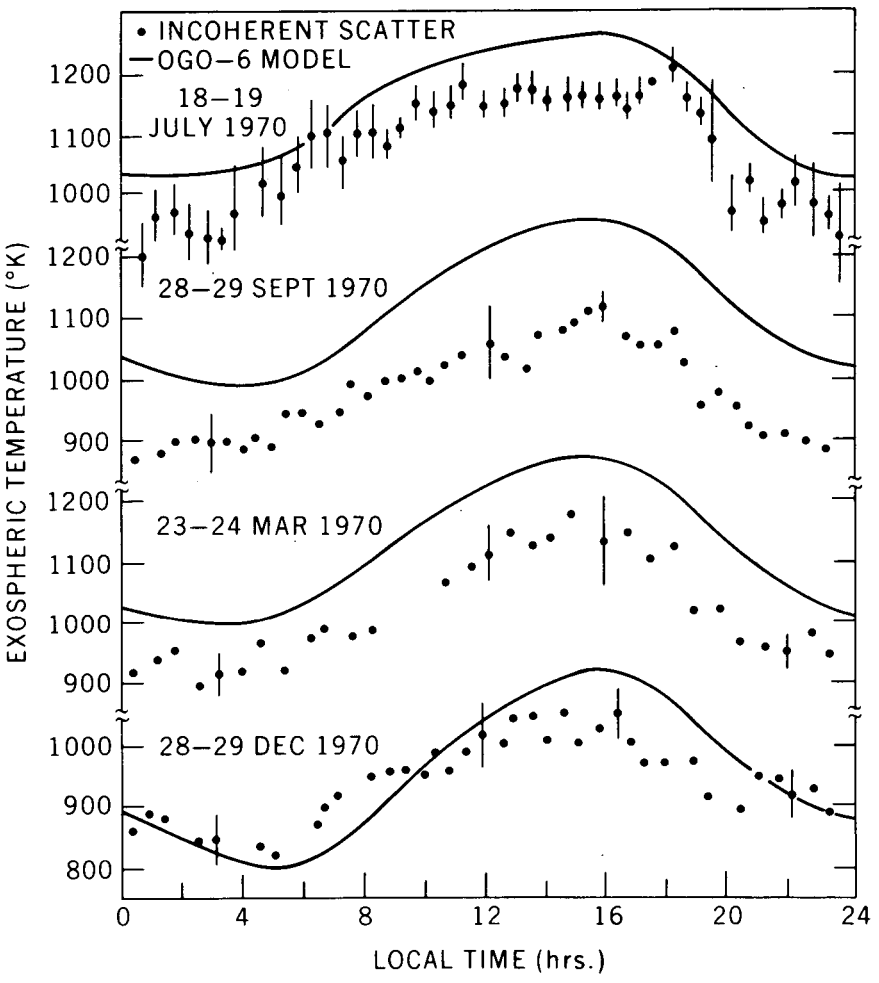

Figure 16b. Diurnal variation of exospheric temperature for incoherent scatter measurements [Salah and Evans, 1972] and the OGO-6 empirical model.

Table 1. Quiet Days with Available OGO-6 Data

1969			1970		
178*	244	362	4	83	234
179	245	363	5	84	236
180	246	364	6	85	280
181	247	365	7	92	282
185	255		11	102	288
186	256		13	103	294
187	265		14	104	308
188	269		15	118	336
189	281		18	127	343
190	288		22	128	350
191	289		23	129	357
192	293		24	130	
199	296		25	131	1971
200	302		26	136	
201	303		27	138	6
202	304		28	139	26
203	305		29	142	132
204	309		38	146	133
205	317		40	156	
206	318		41	157	
210	319		42	160	
213	320		43	161	
214	321		44	162	
218	322		51	163	
223	327		52	173	
226	328		54	174	
227	329		70	175	
228	337		71	176	
233	342		73	180	
234	346		74	181	
236	351		75	196	
237	352		76	197	
240	353		77	200	
241	354		78	214	
242	355		79	215	
243			80	216	
			81	217	
			82	232	

*Daycount from Jan 1

Table 2. Model Coefficients and Errors for 450 km Densities

	N_2		He		O	
a_{20}	-3.23254E-2	± 2.4E-2	4.44944E-2	± 3.8E-2	-1.20421E-1	± 1.3E-2
a_{40}	2.58195E-1	± 2.5E-2	1.22096E-2	3.4E-2	7.53022E-3	1.2E-2
f^{a1}_{00}	9.57068E-3	5.0E-4	2.06281E-4	1.8E-4	6.42065E-3	2.0E-4
f^{a2}_{00}	-5.93446E-5	1.6E-5	-1.02533E-5	6.9E-6	-4.97163E-5	7.5E-6
f^{a1}_{00}	2.59132E-2	1.5E-3	-3.22334E-3	6.9E-4	1.50364E-2	6.0E-4
f_1	-1.92310E-1	3.1E-2	1.0		1.10527E-1	7.6E-2
k^{a}_{00}	2.76819E-2	4.1E-3	-9.24999E-4	4.0E-3	1.35510E-2	2.6E-3
k^{a}_{20}	3.32960E-2	6.9E-3	-4.90310E-2	6.9E-3	-7.96150E-3	4.9E-3
c^{1}_{00}	2.15307E-1	2.2E-2	3.36485E-1	2.1E-2	7.18792E-2	1.5E-2
c^{1}_{20}	8.45427E-2	3.1E-2	-1.21895E-1	2.6E-2	-1.11102E-3	1.7E-2
t^{a1}_{00}	-1.19494E+3	8.0E+0	4.16855E+1	3.4E+0	1.55526E+1	8.0E+0
c^{2}_{00}	2.66389E-1	2.3E-2	4.70517E-1	2.1E-2	2.00090E-1	1.2E-2
C^{2}_{20}	2.64229E-1	4.1E-2	-1.67892E-1	3.0E-2	6.15261E-2	1.9E-2
t^{c2}_{00}	7.87142E-1	1.3E+0	1.02749E+2	1.1E+0	8.65226E+1	1.4E+0
c^{1}_{10}	-1.55170E+0	3.9E-2	1.28528E+0	6.1E-2	-2.73134E-1	1.7E-2
c^{1}_{30}	-3.43730E-1	3.2E-2	1.43196E-1	5.3E-2	-4.95760E-2	1.8E-2
c^{1}_{50}	1.67800E-1	2.4E-2	-1.86156E-1	3.8E-2	-2.06922E-3	1.6E-2
t^{c1}_{10}	-5.96942E+0	9.1E-1	-5.19632E+0	1.1E+0	1.22284E+1	3.0E+0
c^{2}_{10}	-9.17841E-2	3.9E-2	2.13583E-1	2.3E-2	-1.88087E-1	1.4E-2
t^{c2}_{10}	2.11428E+2	1.7E+1	-4.25969E+1	2.5E+0	2.58183E+1	3.2E+0
a_{11}	-8.06862E-1	3.1E-2	-4.23383E-1	2.5E-2	-4.44144E-1	1.6E-2
a_{31}	-7.73657E-2	8.9E-3	5.24724E-3	1.0E-2	-2.24184E-2	5.2E-3
a_{51}	4.29883E-2	5.7E-3	-3.37164E-2	4.0E-3	6.15071E-3	3.3E-3
c^{1}_{11}	-4.91628E-2	4.8E-2	2.79221E-1	3.8E-2	-1.12828E-1	2.5E-2
c^{1}_{21}	-1.62804E-2	1.8E-2	3.74919E-2	2.6E-2	-3.20213E-3	9.1E-3
b_{11}	-8.67463E-1	2.5E-2	2.82148E-1	2.7E-2	-4.15266E-1	1.2E-2
b_{31}	-2.13267E-2	9.7E-3	4.75225E-2	1.2E-2	-9.85268E-3	5.1E-3
b_{51}	2.98442E-2	4.4E-3	-2.96619E-2	5.8E-3	1.40306E-3	3.1E-3
d^{1}_{11}	-1.56457E-1	2.4E-2	3.85313E-2	4.3E-2	-4.50245E-2	1.5E-2
d^{1}_{21}	-1.52550E-1	1.8E-2	2.15832E-2	3.9E-2	2.97480E-3	8.8E-3
a_{22}	1.95106E-2	8.2E-3	4.30024E-2	8.0E-3	1.05858E-2	4.8E-3
c^{1}_{32}	2.93628E-2	4.6E-3	2.70815E-3	6.3E-3	1.15912E-2	2.6E-3
b_{22}	1.97074E-2	7.9E-3	-3.75753E-2	7.7E-3	9.61430E-3	4.1E-3
d^{1}_{32}	1.20904E-2	3.9E-3	-2.62367E-3	4.6E-3	7.82691E-3	2.5E-3
b_{33}	1.29388E-2	1.1E-3	1.81657E-3	1.2E-3	1.92377E-3	6.8E-4
a_{33}	8.06962E-3	1.5E-3	2.94319E-3	1.4E-3	2.32258E-3	8.0E-4
n(450)	2.16257E+6	5.1E+4	3.02168E+6	7.0E+4	6.71664E+7	7.0E+5
Q_f	3.14		0.82		1.08	
N_d	984		871		905	

Table 3. Model Coefficients and Errors for Inferred Exospheric Temperatures and 120 km Densities

	Temperature		He		O	
$\overline{T_\infty}$	1.09746E+3	± 1.1E+1				
a_{20}	2.23450E-3	3.2E-3	3.60004E-2	± 3.8E-2	-9.75916E-2	± 1.2E-2
a_{40}	2.86450E-2	3.1E-3	-1.26407E-2	3.5E-2	-9.79390E-2	1.2E-2
f_{00}^{a1}	1.07969E-3	5.3E-5	-2.86349E-4	1.7E-4	1.89483E-3	2.1E-4
f_{00}^{a2}	-5.11469E-6	1.9E-6	-6.94359E-6	6.6E-6	-2.58559E-5	7.4E-6
f_{00}^{a1}	2.67456E-3	9.8E-5	-4.47270E-3	7.1E-4	3.65676E-3	6.5E-4
f_1	1.0		1.0		1.0	
k_{00}^{a}	4.43908E-3	5.6E-4	-4.98860E-3	4.0E-3	-5.48307E-3	2.5E-3
k_{20}^{a}	5.82154E-3	9.8E-4	-5.32688E-2	6.9E-3	-2.50150E-2	4.8E-3
c_{00}^{1}	2.09161E-2	2.5E-3	-3.43574E-1	2.1E-2	1.21477E-1	1.2E-2
c_{20}^{1}	1.82185E-3	3.8E-3	1.17012E-1	2.6E-2	5.13802E-2	1.7E-2
t_{00}^{C1}	-7.90147E+1	1.0E+1	-1.39608E+2	3.4E+0	5.86078E+1	5.4E+0
c_{00}^{2}	2.89788E-2	3.0E-3	4.47150E-1	2.0E-2	8.59177E-2	1.1E-2
c_{20}^{2}	1.68314E-2	4.7E-3	-1.85922E-1	3.0E-2	-6.06341E-2	1.7E-2
t_{00}^{C2}	8.20221E+1	2.0E+0	1.03883E+2	1.1E+0	9.81965E+1	3.2E+0
c_{10}^{1}	-1.75059E-1	4.8E-3	1.43740E-0	6.1E-2	4.91391E-1	1.9E-2
c_{30}^{1}	-4.55491E-2	3.8E-3	1.76714E-1	5.3E-2	1.42440E-1	1.9E-2
c_{50}^{1}	1.78577E-2	3.3E-3	-2.02116E-1	3.8E-2	-1.29622E-1	1.6E-2
t_{10}^{C1}	-7.74545E+0	1.0E+0	-6.06371E+0	1.0E+0	-1.76764E+1	1.3E+0
c_{10}^{2}	-7.87872E-3	5.2E-3	1.98688E-1	2.3E-2	-1.82094E-1	1.4E-2
t_{10}^{C2}	4.62196E+1	1.8E+1	-4.18924E+1	2.8E+0	2.53553E+1	3.0E+0
a_{11}	-1.00212E-1	3.9E-3	-3.67322E-1	2.5E-2	-3.24214E-2	1.3E-2
a_{31}	-7.99562E-3	1.1E-3	7.02718E-3	1.0E-2	1.09767E-2	4.6E-3
a_{51}	4.12455E-3	7.4E-4	-3.60443E-2	4.0E-3	-1.25240E-2	3.2E-3
c_{11}^{1}	1.01873E-3	6.8E-3	2.75532E-1	3.8E-2	-4.67511E-2	2.2E-2
c_{21}^{1}	5.84192E-3	2.1E-3	5.90788E-2	2.6E-2	2.00992E-3	8.5E-3
b_{11}	-1.04346E-1	3.0E-3	3.55576E-1	2.7E-2	4.65936E-2	1.3E-2
b_{31}	-3.29270E-3	1.2E-3	5.00220E-2	1.2E-2	-2.49572E-3	5.2E-3
b_{51}	4.21772E-3	6.3E-4	-3.32297E-2	5.8E-3	-2.03136E-2	3.0E-3
d_{11}^{1}	-1.87679E-2	3.6E-3	6.56431E-2	4.3E-2	2.03699E-2	1.5E-2
d_{21}^{1}	-1.15860E-2	2.1E-3	3.88636E-2	3.9E-2	7.94588E-2	9.3E-3
a_{22}	-5.41524E-4	1.1E-3	3.73572E-2	8.1E-3	3.29472E-3	4.6E-3
c_{32}^{1}	2.58162E-3	6.1E-4	9.67275E-4	6.4E-3	1.03342E-2	3.0E-3
b_{22}	5.70467E-3	1.0E-3	-4.09051E-2	7.8E-3	-4.27613E-3	3.8E-3
d_{32}^{1}	1.04937E-3	5.1E-4	-2.32445E-3	4.6E-3	1.63277E-3	2.2E-3
b_{33}	1.71030E-3	1.5E-4	6.91634E-4	1.2E-3	-4.84872E-3	6.8E-4
a_{33}	1.08499E-3	1.8E-4	2.00630E-3	1.4E-3	-8.24512E-4	7.6E-4
S	2.15093E-2	1.1E-3				
n(120)	3.0 E+11		2.72880E+7	6.3E+5	8.97076E+10	9.0E+8
Q_f	3.05		0.82		1.05	
N_d	984		872		905	

Table 4. Model Coefficients for Inferred Exospheric Temperature Based on Different Time Periods

n(120) -1.09877E-3 ± 3.5E-1
-1.11568E-3 ± 1.1E-1
n(120) -1.11568E-3 ± 1.1E-1 -1.09877E-3 ± 3.5E-1

	27 June 1969 to 4 Aug 1970		29 June 1970 to 13 May 1971	
$\overline{T_\infty}$	1.11568E+3 ±	1.1E+1	1.09877E+3 ±	3.5E+1
a_{20}	4.55397E-3	3.5E-3	-8.71478E-3	4.1E-2
a_{40}	2.59769E-2	2.7E-3	2.22340E-2	1.1E-2
f_{00}^{a1}	1.12636E-3	4.3E-5	1.46310E-3	2.3E-4
f_{00}^{a2}	-6.14146E-6	1.6E-6	-2.34289E-5	7.6E-6
$\overline{f_{00}^{a1}}$	1.81034E-3	4.7E-4	2.90716E-3	7.1E-4
k_{00}^{a}	3.67972E-3	5.7E-4	1.64373E-3	6.9E-4
k_{20}^{a}	4.91533E-3	1.1E-3	3.79008E-3	1.2E-3
c_{00}^{1}	2.34466E-2	6.0E-3	-1.89772E-3	2.7E-2
c_{20}^{1}	6.21293E-3	4.5E-3	-3.77918E-2	3.0E-2
t_{00}^{c1}	-6.97931E+1	1.2E+1	-2.37760E+0	3.7E+1
c_{00}^{2}	2.65288E-2	3.2E-3	-1.58230E-4	2.1E-2
c_{20}^{2}	1.50036E-2	4.3E-3	9.34394E-3	3.7E-2
t_{00}^{c2}	9.69683E+1	3.2E+0	1.39853E+2	1.6E+2
c_{10}^{1}	-1.63496E-1	5.4E-3	-1.42320E-1	2.4E-2
c_{30}^{1}	-4.62570E-2	3.8E-3	-5.52283E-2	1.8E-2
c_{50}^{1}	1.68539E+2	3.1E-3	1.38372E-2	6.2E-3
t_{10}^{c1}	-9.81137E+0	1.1E+0	-1.78368E+0	3.5E+1
c_{10}^{2}	3.84413E-3	1.0E-2	-3.51160E-2	2.5E-2
t_{10}^{c2}	2.62201E+1	3.8E+3	-2.09545E+0	2.8E+1
a_{11}	-1.00840E-1	4.3E-3	-1.11487E-1	2.1E-2
a_{31}	-8.81511E-3	1.0E-3	-2.99367E-3	7.8E-3
a_{51}	3.04996E-3	6.7E-4	2.89507E-3	1.5E-3
c_{11}^{1}	-4.32113E-3	7.5E-3	8.98341E-3	2.0E-2
c_{21}^{1}	1.13675E-2	2.1E-3	2.61265E-2	8.1E-3
b_{11}	-9.75982E-2	3.0E-3	-1.00533E-1	3.2E-2
b_{31}	-4.06116E-3	1.0E-3	4.32731E-3	3.9E-3
b_{51}	3.07876F-3	5.5E-4	2.06197E-3	1.3E-3
d_{11}^{1}	-5.69528E-3	3.1E-3	-2.59543E+2	3.2E-2
d_{21}^{1}	-1.22704E-2	2.0E-3	-1.46737E-3	8.6E-3
a_{22}	1.27142E-4	1.2E-3	1.40907E-3	8.0E-3
c_{32}^{1}	2.67250E-3	7.3E-4	4.23722E-3	2.4E-3
b_{32}	5.13250E-3	9.6E-4	5.51530E-3	3.5E-3
d_{32}^{122}	1.90120E-3	4.5E-4	2.16673E-3	2.3E-3
b_{33}	1.27724E-3	1.3E-4	1.61326E-3	7.9E-4
a_{33}	1.09527E-3	1.8E-4	2.23838E-3	8.6E-4
S	2.05681E-2	9.7E-4	1.98619E-2	3.8E-3
n(120)	3.0 E+11		3.0 E+11	
Q_f	2.38		1.58	
N_d	856		173	

☆ U.S. GOVERNMENT PRINTING OFFICE: 1972-735-966/492